Microfield dynamics in dense hydrogen plasmas with high-Z impurities

Stefan P. Hau-Riege and Jon Weisheit

Phys. Rev. E **95**, 013204 — Published 9 January 2017

DOI: 10.1103/PhysRevE.95.013204

Microfield dynamics in dense hydrogen plasmas with high-Z impurities

Stefan P. Hau-Riege[1] *and Jon Weisheit*[2]
[1] Lawrence Livermore National Laboratory
[2]Department of Physics & Astronomy, Rice University

ABSTRACT

We use large-scale classical molecular dynamics to determine microfield properties for several dense plasma mixtures. By employing quantum statistical potentials (QSPs) to regularize the Coulomb interaction, our simulations follow motions of electrons as well as ions for times long enough to track relaxation phenomena involving both types of particles. Coulomb coupling, relative to temperature, of different pairs of species in the hot, dense matter being simulated ranges from weak to strong. We first study the effect of such coupling differences, along with composition and QSP differences, on the roles of electrons and various mixture components in determining probability distributions of instantaneous, *total* microfields experienced by the ions. Then, we address two important dynamical questions: (1) how is the *quasi-static* part of the total field to be extracted from the time-dependent simulation data; and, (2) under what conditions does the commonly used approximation of ions with fixed Yukawa-like screening by free electrons accurately describe quasi-static fields? We identify a running, short-time average of the total field at each ion as its slowly evolving, quasi-static part. We consider several ways to specify the averaging interval, and note the influence of ion dynamics in this issue. When all species are weakly coupled, the quasi-static fields have probability distributions agreeing well with those we obtain from simulations of Yukawa-screened ions. However, agreement deteriorates as the coupling between high-Z ions increases well beyond unity, principally because the Yukawa model tends to underestimate the true screening of close high-Z pairs. Examples of this fact are given, and some consequences for the high-field portions of probability distributions are discussed.

I. INTRODUCTION

Research on the statistical properties of an $\mathcal{N}$-body system's internal fields dates to Holtsmark's seminal paper on uncorrelated particles, published almost a century ago [1,2]. In recent times much effort has focused on understanding electric microfields in high-density plasmas, where correlations among charged particles are significant, and the internal fields are large. Motivating that work has been the subject's intrinsic theoretical interest – see, e.g., the comprehensive review by Demura [3] – as well as the role of microfields in spectral line broadening and plasma diagnostics [4,5].

The use of classical molecular dynamics (MD) to perform numerical "experiments" is a newer tool for determining plasma microfields. All-particle MD [6-10], with explicit ions *and* electrons, can tackle time-dependent microfield questions beyond the capability of Monte Carlo and most theoretical methods, and provide benchmark data for evaluating various aspects of other, more limited approaches. Our code is a derivative of *ddcMD*, the MD code at the center of Lawrence Livermore National Laboratory's Cimarron Project [11]. Research described in this paper continues that of our earlier publication [10, subsequently referred to as Paper I], in which we used MD to investigate microfields in fully ionized, solid density C – H plasmas. Here, we study hot, compressed hydrogen plasmas doped with

highly charged ions, Ar^{+18} or Kr^{+36}. To insure adequate statistics for mixtures, the typical size of our simulations far exceeds what has been reported elsewhere: minority species have at least 10^4 particles, and majority species, as many as 10^7. Moreover, up to 10^7 time-steps are used to accurately track electron trajectories over the intervals needed to fully characterize time-dependent quantities of interest.

Several facilities [e.g., 12-14] can produce the high energy density conditions that are our focus: total nucleon densities of normal or compressed solids, $N_{ion} \geq 10^{23} cm^{-3}$, and temperatures T (in energy units) hot enough to eliminate electron degeneracy and justify a classical treatment of particle dynamics, $T > T_{Fermi} \approx 8(N_e / 10^{23} cm^{-3})^{2/3} eV$. We assume thermal equilibrium conditions and we restrict our attention to plasmas that are essentially fully ionized, thereby minimizing the effects of any bound states. Charge neutrality gives the electron density as $N_e = \langle Z \rangle N_{ion}$, where $\langle Z \rangle$ is the mean ion charge. We use the Saha-Boltzmann equation [4,5] to estimate H^+ plasma temperatures at which impurity ions with the largest nuclear charge $Z_{\max} e$ will be almost fully stripped. According to it, the abundance of the impurity's bare nucleus exceeds that of its hydrogenic ion when, approximately, the temperature-dependent factor $\left[\left(T / Z_{\max}^2 I_H \right)^{3/2} \exp\left(-Z_{\max}^2 I_H / T \right) \right]$ exceeds $\left(N_e / 10^{23} cm^{-3} Z_{\max}^3 \right)$, with $I_H = 13.6 eV$ being the hydrogen ionization potential. For the plasmas of interest here, this degree of ionization requires temperature values $T \approx \frac{1}{4} Z_{\max}^2 I_H$, or higher, values about an order of magnitude above what is required by the non-degeneracy constraint of classical MD.

Consider a large number of ions of species ν in an isolated, equilibrium plasma. Their fundamental microfield quantity is $W_\nu(\vec{F}_{tot})$, the probability distribution of the total field $\vec{F}_{tot}$ being experienced by any one of them. Although these fields represent a stochastic process, viz., each $\vec{F}_{tot} = \vec{F}_{tot}(t)$, the distribution of their instantaneous values is stationary and can be defined in terms of an ensemble average $\langle ... \rangle_\nu$ with respect to species ν. Thus, in an MD simulation one computes, at any convenient reference time,

$$W_\nu(\vec{F}_{tot}) = \left\langle \delta\left[\vec{F}_{tot} - \sum\nolimits_j \vec{f}_j \right] \right\rangle_\nu \ , \qquad (1)$$

where $\vec{f}_j$ is the field contribution of plasma particle "j", and the sum runs over all but the particle in question. Because isolated equilibrium systems are isotropic, we focus instead on field strengths and their simpler distribution,

$$P_\nu(F_{tot}) = 4\pi F_{tot}^2 W_\nu(\vec{F}_{tot}) \ . \qquad (2)$$

A plasma simulation provides data representing a sample of the unknown $P_\nu(F_{tot})$, as well as information about the contributions of different species to the total field. As is customary, we refer to our MD samples themselves as the probability distributions. In a mixture, there are multiple species, constituent fields, and probability distributions, which

complicates the issue of notation. We use "$P_\nu(F_X)$" to designate whatever is the (sampled) probability distribution of fields of type F_X being experienced by an ion of species ν; P_ν is *not* some particular function with various fields as possible arguments.

Electrostatic forces must be computed at every time step, so all-particle MD generates the field history $\vec{F}_{tot}(t)$ of every charge. Hence, simulations also can provide the autocorrelation function for the total field at ions of each species ν,

$$\begin{aligned} A_\nu(t_2 - t_1) &= \left\langle \vec{F}_{tot}(t_2 - t_0) \cdot \vec{F}_{tot}(t_1 - t_0) \right\rangle_\nu \Big/ \left\langle \vec{F}_{tot}(t_0) \cdot \vec{F}_{tot}(t_0) \right\rangle_\nu \\ &= \left\langle \vec{F}_{tot}(t_2 - t_1) \cdot \vec{F}_{tot}(0) \right\rangle_\nu \Big/ \left\langle \vec{F}_{tot}(0) \cdot \vec{F}_{tot}(0) \right\rangle_\nu \end{aligned} , \tag{3}$$

The second expression for this normalized form of A_ν follows from its properties of stationarity and time-translational invariance [15]. As yet, theoretical models of these functions treat explicitly the ion or the electron sub-system, but not both [see, e.g., 16-18].

The large ion/electron mass ratio suggests a qualitative separation, by timescale, of effects of the local field $\vec{F}_{tot}(t)$ on a radiating plasma ion [4,5]. A quasi-static field $\vec{F}_{slow}(t)$, which represents an aggregate of low-frequency Fourier components of $\vec{F}_{tot}(t)$, can be treated as a source of Stark level shifts. The aggregate of the remaining, high-frequency components, $\vec{F}_{fast}(t) = \vec{F}_{tot}(t) - \vec{F}_{slow}(t)$, can be treated as a collisional broadening flux. Baranger and Mozer [19] proposed a static-ion approximation of the low-frequency microfields, to be determined as follows. First, for a given configuration of all plasma charges, calculate total fields at locations of interest, say, at ions of a certain species ν. Then, keeping all plasma ions fixed, average these instantaneous fields over times "long compared to typical electronic relaxation times, but short compared to ionic times;" this incorporates the average effect of screening by the mobile electrons into a composite, static screened field $\vec{F}_{scr}$ at each ion. Last, perform a configurational average of the static fields $\vec{F}_{scr}$ with respect to ion species ν to obtain its probability distribution $P_\nu(F_{scr})$. The use of such a distribution to describe the influence of (screened) plasma ions on the ensemble of radiators, together with an impact treatment of collision events to describe the remaining influence of plasma electrons on that ensemble, has come to be known as the "standard theory" of Stark broadening [20,21]. Electrons participate on both timescales, so their effects must be handled self-consistently (see [4,22] for discussion of this point).

Our first main task is establishing the link between Baranger and Mozer's field $\vec{F}_{scr}$ and the total field $\vec{F}_{tot}(t) = \vec{F}_{ion}(t) + \vec{F}_e(t)$ at each ion. The screened field determined by their *ansatz* is

$$\vec{F}_{scr} = \frac{1}{\tau}\int_0^\tau dt \left\{ \vec{F}_{tot}(t) \right\}_{\substack{fixed \\ ions}} = \vec{F}_{ion}(0) + \frac{1}{\tau}\int_0^\tau dt \left\{ \vec{F}_e(t) \right\}_{\substack{fixed \\ ions}} \quad . \tag{4}$$

If this $\vec{F}_{scr}$ is to be plausibly quasi-static, the interval τ must be both long enough for a configuration of ions, fixed at their time $t = 0$ positions, to acquire steady electron screening,

and short enough that consequences of ion motions are ignorable. In real plasmas the ion positions are never fixed, of course, and the *quasi-static* field readily obtained from an all-particle simulation,

$$\begin{aligned}\vec{F}_{slow}^{[\tau]} &= \frac{1}{\tau}\int_0^\tau dt\ \vec{F}_{tot}(t) \\ &= \vec{F}_{scr} + \frac{1}{\tau}\int_0^\tau dt\ \left[\vec{F}_{ion}(t) - \vec{F}_{ion}(0)\right] + \frac{1}{\tau}\int_0^\tau dt\ \left[\vec{F}_e(t) - \left\{\vec{F}_e(t)\right\}_{\substack{fixed \\ ions}}\right]\end{aligned} \quad , \tag{5}$$

represents the actual short-time average of dynamically-screened ion fields. This slow field includes corrections to $\vec{F}_{scr}$ due to ion motions that are contemporaneous with electron relaxation, and generally depends on the duration of the averaging. To our knowledge the slow field of Eq. (5) was studied first by Calisti and collaborators [6,7], in their MD simulations of hydrogen plasmas.

Here, we continue to investigate the important question featured in our study of C^{+6} – H^+ plasmas [10]: How should τ be chosen so that $\vec{F}_{slow}^{[\tau]}$ is consistent with the Baranger-Mozer *ansatz* and the separation of Stark effects in the standard theory? In this work, we associate relaxation timescales with the usual plasma frequencies,

$$t_e^{-1} = \omega_e = \left(4\pi e^2 N_e / m_e\right)^{1/2}, \quad t_{ion}^{-1} = \omega_{ion} = \left(4\pi e^2 N_{ion} \sum\nolimits_\nu \xi_\nu Z_\nu^2 / M_\nu\right)^{1/2} \ , \tag{6}$$

where the summation runs over all ion species $Z_\nu e$, whose densities are $N_\nu = \xi_\nu N_{ion}$. The electrons, with charge and mass $(-e, m_e)$, have $\xi_e = \langle Z \rangle$. If a hydrogen plasma contains heavy elements that are fully stripped, or nearly so, the impurity masses are $M_\nu \approx 2Z_\nu M_H$ and a good estimate of the ion timescale is $t_{ion} \approx 60 t_e \left[\xi_e / \left(\xi_e + \xi_H\right)\right]^{1/2}$. Therefore, a rather broad temporal range, $1 \le \omega_e \tau \le 60$, is of interest.

Most theoretical methods for carrying out the configuration average of Eq. (1) are limited to situations wherein characteristic pair interaction energies are small relative to temperature, and correlations represent modest perturbations of an ideal gas [3,19,23]. In that circumstance, the lowest-order results of static electron screening are explicit [22]: The total interaction energy for the plasma is a sum of ion-pair terms u_{ij}^Y involving the familiar Yukawa (or, Debye-Huckel) potential,

$$u_{ij}^Y\left(r = \left|\vec{r}_i - \vec{r}_j\right|\right) = Z_i e \phi_j^Y(r) = \left(Z_i Z_j e^2 / r\right) \exp\left(-r / D_e\right) \ , \tag{7}$$

with $D_e = \left(T / 4\pi e^2 N_e\right)^{1/2}$; and, the field $\vec{F}_{scr}(\vec{r}_i)$ at each ion $Z_i e$ is a sum of individual Yukawa fields,

$$\vec{F}_{scr}(\vec{r}_i) = \sum_{j \in ions} \vec{f}_j^Y = -\sum_{j \in ions} \vec{\nabla}_i \phi_j^Y\left(\left|\vec{r}_i - \vec{r}_j\right|\right) \quad . \tag{8}$$

Simplifications leading to these Yukawa formulae are not valid when correlations are strong, and identifying actual limitations of the Yukawa picture is this paper's second main task. High-Z – low-Z plasma mixtures are well suited to this task because they exhibit a range of correlations, as gauged by Coulomb coupling constants for different pairs of species [e.g., 5,8],

$$\Gamma_{ss'} = |Z_s Z_{s'}| \left(e^2 / aT \right) \left[\left(\xi_s + \xi_{s'} \right) / \left(1 + \delta_{ss'} \right) \right]^{1/3} \quad . \tag{9}$$

Here, indices s, s' denote either electrons (e) or ions (ν), and the characteristic inter-particle spacing a is defined by the total ion density, $4\pi a^3 N_{ion} / 3 = 1$. Correlations among electrons and protons in our hot, dense plasmas are weak enough $(\Gamma \sim 0.01)$ so that the Yukawa model certainly would be valid for pure hydrogen. But, correlations among high-Z impurity ions are strong $(\Gamma > 1)$, and those between the impurities and the electrons or protons are moderate $(\Gamma \sim 0.1)$. At present, all-particle simulations are the only way to faithfully capture all the correlation effects in such systems.

Results described in Section II explore consequences of mixed Γ-values for distributions of total microfields. Numerous all-particle MD simulations performed for the purpose of identifying τ *a posteriori* are presented and discussed in Section III, and – because none of these is wholly satisfactory – an improved model for calculating τ *a priori* is developed in Section IV. In Section V we compare statistical information about slow fields computed from full dynamical information with similar information about fields of ions having the fixed, Yukawa form of electron screening. These comparisons, which involve equivalent MD simulations as well as equivalent hypernetted-chain (HNC) calculations [15], quantify certain limitations of the static screening model. (In Yukawa MD simulations the individual fields $\vec{F}_{scr}$ change on a timescale $\sim t_{ion}$, but again have stationary statistical properties.) Finally, in Section VI we review our main results and note some prospective inquiries. Throughout, emphasis is placed on identification and understanding of significant features and trends shown by this set of large-scale plasma simulations.

II. TOTAL MICROFIELDS IN HIGH-Z – LOW-Z PLASMA MIXTURES

This section treats the rapidly changing, instantaneous fields $\vec{F}_{tot}(t)$ experienced by ions. Using results from several all-particle MD simulations, we discuss how changes in QSP, N_{ion}, T, or impurity concentration affect the contributions of different plasma species to $P_\nu(F_{tot})$. Also, we describe specific microfield features attributable to electrons that do not arise in MD calculations involving static-screened ions. Both of these topics help explain details of the quasi-static distributions $P_\nu(F_{slow}^{[\tau]})$ we subsequently obtain for these plasmas.

A. The Role of Quantum Statistical Potentials

For classical, all-particle MD it is necessary that some short-range modification of the Coulomb interaction be selected to prevent the steady collapse of the electrons onto the ions. This is commonly done by the introduction of quantum statistical potentials (QSPs)

that mimic, in a statistical sense, the effects of diffraction and wave function anti-symmetry that would be exhibited by electrons subjected to a quantum description [24,25]. Experience within the Cimarron Project, involving a wide range of dense plasma phenomena [11,26-29], has shown the importance of determining how MD results are affected by the use of, and choice of, a QSP. In Paper I we examined the QSP-related sensitivity of microfield properties for various carbon plasmas, and now we reconsider those findings for microfields in high-Z – low-Z mixtures.

The standard QSP set for our simulations has the Dunn-Broyles interaction to account for diffraction effects [30], and a second term for anti-symmetry effects in electron-electron interactions [31], viz.,

$$u_{ss'}^{DB}(r) = \left(\frac{Z_s Z_{s'} e^2}{r}\right)\left[1 - \exp\left(\frac{-2\pi r}{\Lambda_{ss'}}\right)\right] , \tag{10}$$

$$u_{ss'}^{S}(r) = \delta_{se}\delta_{s'e}(\ln 2)T \exp\left[\frac{-4\pi r^2}{(\ln 2)\Lambda_{ss'}^2}\right] , \tag{11}$$

where $\Lambda_{ss'} = \sqrt{2\pi\hbar^2 / \mu_{ss'}T}$ is the thermal de Broglie wavelength for a particle whose mass is the reduced mass of the pair (s,s'). (In Paper I this combination was denoted "DB+S.") Our alternative potential for sensitivity studies has been used in MD simulations by Calisti, Talin, and co-workers [32,33]. Strictly speaking, it is not a QSP. In lieu of a temperature-dependent diffraction term, it employs a phenomenological formula,

$$u_{ev}^{CT}(r) = \left(-Z_v e^2 / r\right)\left[1 - \exp(-r/\delta_v)\right] , \tag{12}$$

with $\delta_v = Z_v e^2 / I_v$, that keeps the electron-ion interaction $u_{ev}^{CT}(r)$ for the pair (e, Z_v) from exceeding that pair's binding energy I_v; no other Coulomb modifications are introduced.

Different T- and Z-dependences are found among various QSP sets in use, and temperatures fixed by our ionization balance requirements for the plasma's most highly charged impurities ($T \approx \frac{1}{4} Z_{\max}^2 I_H$) can highlight these differences. For example, every set has an electron-ion pair interaction that is finite in the limit $(r \to 0)$. This leads to a finite value for the maximum electron density enhancement at an ion Z_v, as specified by the pair distribution function $g_{ev}(0) = \exp\left[-U_{ev}^{MF}(0)/T\right]$, where $U_{ev}^{MF}(0) = u_{ev}^{pair}(0) + \Delta I_v$ is the limiting value of the potential of mean force between electrons and ions Z_v, and where the small positive correction ΔI_v to the pair interaction accounts for continuum lowering (see [27,34], and Sec. IV). It also leads to a maximum strength of the instantaneous field f_e any electron can produce at that ion. By ignoring ΔI_v, our standard QSP choice (Dunn-Broyles) for u_{ev}^{pair} gives

$$g_{ev}^{DB}(0) \approx \exp\left[\sqrt{4\pi Z_v^2 I_H / T}\right] \ , \ \text{and} \ \ f_e^{DB} \le (\pi T / 2I_H) F_0 \ , \tag{13}$$

while the Calisti-Talin potential gives

$$g_{ev}^{CT}(0) \approx \exp\left[Z_v^2 I_H / T\right] \ , \ \text{and} \ f_e^{CT} \le (Z_v^2 / 8) F_0 \ , \tag{14}$$

where $F_0 = e / a_0^2 = 27.2 \ V / a_0$ is the atomic unit of field strength. Under all conditions, these finite maximum values operate so as to reduce the computed likelihood of very strong total *electron* fields $\vec{F}_e$ at an ion. However, in hot, high-Z – low-Z mixtures their overall effect on microfield distributions may be more complicated than those found for carbon plasmas, because the temperature factor $(T / Z_v^2 I_H) \sim (Z_{\max} / Z_v)^2$ can be large or small.

B. Distributions of Total Fields and of Fields of Mixture Components

Our first set of all-particle simulations for mixed-Γ systems involves three different H^+ plasmas having a small concentration of Kr^{+36} ions, $\xi_{Kr} = 0.01$. These MD computations have 99×10^4 protons and 1×10^4 krypton ions, plus 1.35×10^6 electrons. Table 1 lists the temperature and total ion density, plus several associated physical quantities for these simulations, therein labeled Kr1, Kr3 and Kr4.

The top panels of Fig. 1 show total microfield probability distributions at Kr^{+36} ions for the three cases, and the bottom panels, corresponding distributions at H^+ ions. Here and throughout this paper we deal principally with scaled fields and their distributions, defined as $\beta_{tot} = F_{tot} / F_0$ and $P_v(\beta_{tot}) = F_0 P_v(F_{tot})$. Each panel has one unlabeled curve representing the distribution extracted from a simulation that employs our standard QSPs and a second curve (labeled "CT") for the distribution resulting from a comparable simulation that employs the potential of Eq. (12). Each panel also has a third curve that shows the ideal-gas limit $(T \to \infty)$ of the distribution for that plasma – the familiar Holtsmark function for uncorrelated charges having Coulomb fields,

$$H(\beta) = (2 / \pi\beta) \int_0^\infty dx \ x \sin(x) \exp\left[-(xF_H / F_0 \beta)^{3/2}\right] . \tag{15}$$

In an ideal plasma mixture, every species "s" (electron or ion) experiences this same distribution, whose normal field $F_H = (8\pi / 25)^{1/3} Z_{MIX} e / a^2$ involves an effective charge

$$Z_{MIX} = \left[\sum\nolimits_s \xi_s |Z_s|^{3/2}\right]^{2/3} . \tag{16}$$

Inclusion of the Holtsmark distribution reveals the extent to which correlations affect a given set of results, and facilitates comparisons among various distribution plots for different species, mixtures or conditions.

Several comments can be made regarding Fig. 1. First, none of these MD results for the total microfield differ greatly from their corresponding Holtsmark distributions. As

expected, the differences do increase when there is a large jump in plasma density and, hence, a substantial increase in particle correlations: compare panels (a) and (b), and (d) and (e), and also notice the large scale differences for β -values. The MD results change less when the temperature drops from 10 to 5 keV, even though Eq. (13) suggests strong T-dependence. For a charge-neutral plasma the main effect of a modest temperature drop is some increase (decrease) in the density of electrons (ions) near an ion of charge $Z_v e$. And, for example, if we could approximate all pair distribution functions at small r by their linearized form, viz., $g_{ss'}(r) \to [1 - u_{ss'}^{pair}(r)/T]$, then a fractional temperature change $\Delta T / T$ would cause the total charge density ρ_{tot} near $Z_v e$ to change only by a proportional amount,

$$\left[\Delta\rho_{tot}(T;r)/\rho_{tot}(T;r)\right]_v \propto \left[-\Delta T/T\right] \quad , \qquad r << a \ , \tag{17}$$

where the positive constant of proportionality depends upon the specific form of the QSP pair interactions. The overall consequence of the temperature drop is that the ion $Z_v e$ experiences a greater likelihood of strong total microfields $\vec{F}_{tot}$ (and a lesser likelihood of weak total fields). Though small, this difference is noticeable in the Kr^{+36} data plotted in panels (b) and (c) of Fig. 1.

Next, in considering the influence of different QSPs, the two Fig. 1 panels for the solid density case ($N_{ion} = 10^{23} cm^{-3}$) indicate that $P_{Kr}(\beta_{tot}) \approx P_H(\beta_{tot}) \approx H(\beta)$, i.e., that this plasma is nearly ideal, and shows negligible QSP sensitivity. The situation for the higher density $H^+ - Kr^{+36}$ plasmas is more complicated, which is the possibility raised in Sec. IIA. The distributions $P_H(\beta_{tot})$ show QSP sensitivity comparable to the differences exhibited in our carbon plasma simulations of Paper I, while the distributions $P_{Kr}(\beta_{tot})$ show less. These differing sensitivities are consequences of the fact that strong *total* fields are due primarily to close electrons, and, in plasmas with $T \approx \frac{1}{4} Z_{\max}^2 I_H$, Eqs. (13) and (14) have the two QSPs giving similar short-range effects for (e, Kr^{+36}) pairs, but very different short-range effects for (e, H^+) pairs. Specifically, for the former, $[g^{DB}(0)/g^{CT}(0)] \approx 20$ and $[\max f_e^{DB} / \max f_e^{CT}] \approx 3$; for the latter, $[g^{DB}(0)/g^{CT}(0)] \approx 1$ and $[\max f_e^{DB} / \max f_e^{CT}] \approx 10^3$.

These and other details about the make-up of the total fields, $\vec{F}_{tot} = \vec{F}_{Kr} + \vec{F}_H + \vec{F}_e$, can be gleaned from the two panels of Fig. 2, in which we use simulation data to "decompose" $P_{Kr}(\beta_{tot})$ and $P_H(\beta_{tot})$ into distributions of their electronic and various ionic components. In this figure and several later ones, the order in which curves are crossed by an arrow matches the order of their labels, listed top to bottom in the legend. It is worth remembering that a distribution $W_v(\vec{\beta}_{ion})$ of ion fields cannot be treated as a convolution of the ion species' individual distributions when ion-ion correlations in the plasma are significant, i.e., $\Gamma \geq \frac{1}{2}$ for ion pairs. (See [8] for discussion of this point with regard to ion and electron fields.) For instance, in this figure the distributions of total fields at Kr ions and at H ions are quite similar, but – because of differing degrees of correlation – the contributions of various species to these total fields clearly are very different.

To investigate the sensitivity of total field distributions to impurity concentrations in a high-Z – low-Z mixture, we carried out simulations for H^+ – Ar^{+18} plasmas having fixed temperature and nucleon density, $T = 1keV$ and $N_{ion} = 10^{24} cm^{-3}$, but varying argon abundance fractions, $\xi_{Ar} = 0.001,\ 0.01,\ 0.10$. Table I also includes relevant physical quantities for these cases (Ar1, Ar2 and Ar3), each of whose simulation has 10^4 impurity ions to maintain good overall statistics. Microfield distributions for these plasmas are plotted in Fig. 3, where the two panels compare $P_{Ar}(\beta_{tot})$ and $P_H(\beta_{tot})$ for the three argon abundances. The most striking result of these simulations is how much the distributions $P_\nu(\beta_{tot})$ change, for both species, when the argon concentration decreases from 0.1 to 0.01, relative to when the decrease is from 0.01 to 0.001. In the first instance, the probability of a strong total field, at H^+ or at Ar^{+18}, is much reduced, and peak microfield distribution values rise by about a factor of 2. In these cases, most of the qualitative difference in the $P_\nu(\beta_{tot})$ curves is caused by the substantial decrease in electron density, from $2.7N_{ion}$ to about $1.2N_{ion}$, that occurs with the first drop in argon concentration. In the second instance, when ξ_{Ar} decreases from 0.01 to 0.001, the relative change in electron density is much less, and peak distribution values rise only by about 10%.

Also shown in Fig. 3 are total field distributions that occur with the use of the alternative interaction, "CT," in the plasma simulation where $\xi_{Ar} = 0.01$. These results reveal a QSP-related sensitivity of $P_\nu(\beta_{tot})$ for both ion species comparable to that due to the Ar abundance change from 0.01 to 0.001. This can be understood by combining the observation, just above, regarding the evolution of both ionic distributions $P_\nu(\beta_{ion})$ as ξ_{Ar} decreases, with earlier comments – in the case of Kr impurities – about the greater sensitivity of $P_H(\beta_{tot})$ to QSPs.

Figure 4, which is analogous to Fig. 2, shows the decomposition of $P_\nu(\beta_{tot})$ at Ar^{+18} and H^+ into the distributions $P_\nu(\beta_s)$ of fields due to the different species present. Certain trends with respect to the argon impurity abundance are discernable. First, electrons always are the main source of strong fields at argon ions, whereas, depending on the value of ξ_{Ar}, one or both ion species as well as the electrons contribute strong fields at hydrogen ions. Also, at both ion species the distribution $P_\nu(\beta_{ion})$ of the scalar ionic field changes from essentially $P_\nu(\beta_{Ar})$ to a distribution much closer to $P_\nu(\beta_H)$ as ξ_{Ar} decreases from 0.1 to 0.001. This goes to the question of how low a species' relative concentration must be for the effects of its ions on microfield properties to be ignorable. It may be that, if its size is large enough, a simulation with impurity concentration not much lower than 0.001 approximates well the convenient theoretical picture of a unique radiator immersed in an otherwise homogeneous plasma, while still providing a credible ensemble average.

III. SLOW MICROFIELDS IN HIGH-Z – LOW-Z PLASMA MIXTURES

The *ansatz* of Baranger and Mozer assumes that electrons establish their static screening clouds around stationary ions. What, if any, averaging interval(s) τ in an all-

particle simulation closely corresponds to this idealized picture? We tackle this question by studying various statistical properties of the slow fields defined by Eq. (5).

A. The τ-Plateau of Slow Microfield Distributions

Calisti *et al* [7] described consequences of different averaging intervals τ in regard to microfields at neutral points (i.e., H *atoms*) in a hydrogen plasma. They used all-particle simulations to compute slow-field distributions for a limited number of relevant τ-values, but identified no particular constraints on the averaging interval. In Paper I, we used numerous distributions $P_C(F_{slow}^{[\tau]})$ for pure carbon plasmas to show continuous evolution with increasing τ throughout the interval $[t_e, t_{ion}]$. However, there was a modest range of τ-values, dubbed the τ-plateau, within which we found little change in the distributions. Such a plateau signifies quasi-static field behavior.

To study the τ-plateau phenomenon in high-Z – low-Z mixtures, we computed MD values of $P_\nu(F_{slow}^{[\tau]})$ for all the plasmas listed in Table 1, and in each case for many τ-values in the interval $\frac{1}{2}t_e \le \tau \le 2t_{ion} \approx 10^2 t_e$. Our standard QSP was used in all these simulations. As τ increases, there is a declining influence of high field configurations (close electrons) due to their rapid motions. Because of this, the distributions become more strongly peaked at weak-field values and less like that plasma's Holtsmark distribution. Panel (a) of Fig. 5 shows results from Paper I for a fully ionized, pure carbon plasma at normal solid density and $T = 200eV$ (case C1); panels (b) and (c) show new results for $H^+ - Ar^{+18}$ and $H^+ - Kr^{+36}$ plasmas having impurity concentrations $\xi_{Ar} = 0.1$ and $\xi_{Kr} = 0.01$ (cases Ar3 and Kr3, respectively). Unlike the pure carbon plasma, in each mixture the distribution of slow microfields evolves steadily with increasing τ throughout the span of averaging intervals considered, and visual inspection of stacked distribution plots yields no obvious τ-plateau. Because this is true for *every* high-Z – low-Z case we simulated, we must turn to the other option developed in Paper I for identifying τ-plateaus.

B. The τ-Plateau of Microfield Autocorrelation Functions

The behavior of the field autocorrelation functions for ions in mixtures is complicated, even when the electrons are treated as a uniform background [17], and as yet we have little understanding of these functions in plasmas with free electrons. In our earlier study, we found that the functions $A_C(t)$ in carbon plasmas are nearly constant at times near the upper end of a range of averaging intervals for which the corresponding distributions $P_C(\beta_{tot})$ exhibit τ-plateau behavior. For an autocorrelation function, such a plateau feature somewhere within $[t_e, t_{ion}]$ also is indicative of stable electron charge density about the ions [7,35]. To check whether plateaus exist for autocorrelation functions of the fields experienced by high-Z impurities, we determined $A_\nu(t)$ for several mixtures and plot some of these results in Fig. 6. Here again, there is an obvious difference between the high-Z impurity results and those for the pure C^{+6} plasma: Panel (a) shows that, some time before $\omega_e t = 1$, autocorrelation curves for the high-Z impurity ions begin to exhibit substantial amplitude fluctuations that obscure any other, detailed feature. These rapid variations are not the numerical noise one would expect with too few impurities in the simulation, because all autocorrelation functions in Figs. 6a and 6b are constructed from data for "ensembles" of

equal size, namely, 10^4 ions. However, the two autocorrelations in Fig. 6a that correspond to plasmas with $N_{ion} = 10^{23} cm^{-3}$ clearly have smaller fluctuation amplitudes than the $A_{Kr}(t)$ curve for the plasma with $N_{ion} = 10^{25} cm^{-3}$, and – other than total ion density – the two H^+ plasmas with Kr^{+36} impurities are the same.

Given this observation, we sought a density-related explanation for the frequent and abrupt spikes in the field autocorrelations of the high-Z impurities. The effort led to the recognition that, even in simulations of our size, the fleeting existence of just one (*e*, high-*Z*) pair whose separation is small enough to produce the maximum field strength of Eq. (13), $f_e^{DB} = (\pi T / 2I_H)F_0$, results in a contribution to $\vec{F}_{tot}$ large enough to momentarily influence the average defining $A_\nu(t)$. Between the two plasmas with Kr^{+36} impurities, the probability of such a close pair increases in proportion to, and only because of, the higher mean density N_{ion}. In other comparisons it might increase primarily as a result of a larger charge Z_ν. The situation is similar to a study of electron dynamics around one fixed, high-Z ion in a uniform density background of positive charge [18]. Its authors found strong, persistent fluctuations in the microfield autocorrelation function of that idealized system, beginning at early times $\omega_e t < 1$. By examining trajectories of individual electrons, their fluctuations in $A_Z(t)$ could be connected with intermittent quasi-bound motions about the charged point Z. Such fluctuations did not occur at a neutral point [7].

We can apply this information to other comparisons involving $A_\nu(t)$ data in Fig. 6. For the two plasmas in Fig. 6a at solid density, $N_{ion} = 10^{23} cm^{-3}$, the very different Z_ν-values give rise to only a modest difference in fluctuations by their corresponding autocorrelation functions. In these plasmas of very different temperature, there are similar (QSP – dependent) density enhancement factors for very close electrons, i.e., $g_{eKr}(0) \approx g_{eC}(0)$, but the mean electron density is nearly a factor of six higher in the pure carbon plasma. Even so, there are larger amplitude fluctuations by $A_{Kr}(t)$, which therefore must be the result of that plasma's much higher temperature enabling much larger individual fields f_e, per Eq. (13).

Figure 6b shows microfield autocorrelation functions at H^+ ions in the compressed plasmas with argon impurity ions. H^+ ions are incapable of producing large local enhancements of the electron density; our QSP gives $g_{eH}(0) \approx 10^{(3/Z_{\max})} < 2$. However, the high temperature of the Ar-doped plasma does make possible strong individual fields f_e of very close electrons, and this is consistent with the H^+ autocorrelation functions having some fluctuations. The most interesting aspect of these curves, though, is the effect of ξ_{Ar} on the behavior of $A_H(t)$ in three, otherwise identical plasmas. The modest plateau-like feature for the case $\xi_{Ar} = 0.1$ that is centered near $\omega_e t = 8$ diminishes as the argon fraction decreases first to 0.01 and then 0.001. The decomposition plots of Fig. 4 reveal that, when $\xi_{Ar} = 0.1$, the ionic field at a hydrogen ion is essentially that produced by Ar^{+18} ions, but when $\xi_{Ar} = 0.001$ it is essentially that produced by other H^+ ions. So, the ability of $A_H(t)$ to exhibit plateau-like behavior apparently depends on which species dominates the total ionic field $\vec{F}_{ion}$ at H^+. (If the analogous situation holds for $A_{Ar}(t)$, that fact is masked by the large fluctuations we observed in those results.)

Overall, then, we found plateau behavior in only two of the many microfield autocorrelations studied – $A_C(t)$ in the pure carbon plasma of Paper I, and $A_H(t)$ in the doped hydrogen plasma with $\xi_{Ar} = 0.1$. In both of these cases, the total ionic field $\vec{F}_{ion}$ at the species in question is dominated by ions with $\xi_\nu Z_\nu > 1$, but it is not clear from the decomposition plots in Figs. 2 and 4 whether this condition alone is sufficient to produce a plateau feature.

C. The τ-Plateau of the Second Moment of Slow Microfield Distributions

We focus next on whether just the mean squared quasi-static microfield is a quantity useful for identifying optimal τ–values. The set of carbon distributions $P_C(F_{slow}^{[\tau]})$ displayed in Fig. 5a suggests that the change of the second moment $\left\langle \vec{F}_{slow}^{[\tau]} \cdot \vec{F}_{slow}^{[\tau]} \right\rangle_C$ with respect to τ should be small in the plateau region because, then, distributions are closely matched at the more probable β-values. Simulation results plotted in Fig. 7 confirm that expectation for the carbon plasma with $\xi_C = 1$. The scaled quantity $\left\langle \beta_{slow}^2(\tau) \right\rangle_C \equiv \left\langle \vec{F}_{slow}^{[\tau]} \cdot \vec{F}_{slow}^{[\tau]} \right\rangle_C \Big/ F_0^2$ decreases by about a factor of 5 over the interval $1 \le \omega_e \tau \le 10^2$, with a slope that is noticeably smaller in the region $2 < \omega_e \tau < 20$. However, the other curves in Fig. 7, for mixtures also treated in Fig. 5, do not evince a $\left\langle \beta_{slow}^2(\tau) \right\rangle_\nu$ plateau for fields at the highly charged impurity ions. Instead, collectively they suggest a trend for decreasing ξ_ν-values of increasing $\left\langle \beta_{slow}^2(\tau) \right\rangle_\nu$ slopes in the region around $\omega_e \tau = 10$.

In spite of the differences noted among the autocorrelation functions $A_\nu(t)$ in Fig. 6, and among the second moments $\left\langle \beta_{slow}^2(\tau) \right\rangle_\nu$ in Fig. 7, all these time-dependent curves exhibit a common form. Near t_e, there is a marked drop as the electrons' motions causing their initial configuration to disassemble; then, near t_{ion} there is a second drop toward zero as the initial ionic configuration also disassembles. Between these drops, where an actual plateau would signify distinct separation of electron and ion dynamical effects, is an interlude of more gradual decline. In fact, these two ensemble averages are closely related, and a simple calculation yields the connection. First, differentiate the quotient,

$$B_\nu(\tau) = \left\langle \vec{F}_{slow}^{[\tau]} \cdot \vec{F}_{slow}^{[\tau]} \right\rangle_\nu \Big/ \left\langle \vec{F}_{tot} \cdot \vec{F}_{tot} \right\rangle_\nu = \left\langle \beta_{slow}^2(\tau) \right\rangle_\nu \Big/ \left\langle \beta_{tot}^2 \right\rangle_\nu \ , \tag{18}$$

with respect to the averaging interval τ, using the slow microfield's definition, Eq. (5). By using properties of the microfield autocorrelation function noted earlier, the result can be re-written in the compact form

$$\frac{\tau}{2} \frac{dB_\nu(\tau)}{d\tau} + B_\nu(\tau) = \frac{1}{\tau} \int_0^\tau dt \ A_\nu(t) \ , \tag{19}$$

with $B_\nu(0)=1$ being the initial condition for this dimensionless quantity. The right hand side of Eq. (19) can be viewed as a "slow" autocorrelation function, $\left(A_{slow}^{[\tau]}\right)_\nu$ that smoothes out strong, transient effects of close electron-ion encounters once $\omega_e\tau \sim 1$.

Now, suppose there exists a range of times τ within which the autocorrelation function is constant, i.e., $A_\nu(\tau)=A_\nu(\tau_1)$ for $\tau_1 \le \tau \le \tau_2$. Equation (19) reveals that the co-existence of a $\left\langle \beta_{slow}^2(\tau)\right\rangle_\nu$ plateau somewhere within that range, say, in $[\tau_a,\tau_b]$, where $\tau_1 \le \tau_a < \tau_b \le \tau_2$, would require $\left(A_{slow}^{[\tau_1]}\right)_\nu = A_\nu(\tau_1)$. When this requirement is satisfied, the constant values $B_\nu(\tau)$ and $A_\nu(\tau)$ are identical throughout $[\tau_a,\tau_b]$, and it follows that $A_\nu(\tau)=A_\nu(\tau_1)$ for all earlier times $0 \le \tau \le \tau_1$. In other words, the autocorrelation function's plateau must extend to the larger interval $0 \le \tau \le \tau_2$, and therefore must have the value $A_\nu(\tau_1)=A_\nu(0)=1$. But, it is known that the microfield autocorrelation function is not constant at early times [15,36]; thus, concurrent plateaus by $B_\nu(\tau)$ and $A_\nu(\tau)$ can be ruled out. When $A_\nu(\tau)$ has no plateau feature, Eq. (19) shows that the second moment $\left\langle \beta_{slow}^2(\tau)\right\rangle_\nu$ still evolves without a plateau as τ increases.

D. The τ-Plateau and Ion Dynamics

The smaller the slope that the second moment $\left\langle \beta_{slow}^2(\tau)\right\rangle_\nu$ exhibits somewhere within the interval $1<\omega_e\tau<60$, the more realistic the concept of static-screened microfields is for that dynamical system. However, if $\left\langle \beta_{slow}^2(\tau)\right\rangle_\nu$ exhibits a persistent decline at times $\tau > 1/\omega_e$, we can infer that the influence of ion motions is ongoing. This knowledge, together with the earlier comments about the ion dominating $\vec{F}_{ion}$, prompted us to simulate another 10 keV H^+ plasma with a Kr^{+36} impurity $(\xi_{Kr}=0.01)$, but with the hydrogen mass being changed to match that of krypton. Some results for this "heavy H" plasma are shown in Fig. 8. A comparison of these slow field distributions at Kr^{+36} with those in Fig. 5c reveals considerably more bunching among the heavy-H curves for $P_{Kr}(\beta_{slow}^{[\tau]})$ with $\tau = 6.8, 16, 39$; changes among these distributions are now like the pure carbon plasma results of Fig. 5a. Additionally, the dashed, heavy-H curve in Fig. 7 enables us to contrast the time-dependence of $\left\langle \beta_{slow}^2(\tau)\right\rangle_{Kr}$ for plasmas with different hydrogen mass that are otherwise the same. Both of these heavy-H features argue for plateau-like behavior of a slow microfield distribution being the consequence of all ion species important for $\vec{F}_{ion}$ having large masses, $M_\nu >> M_H$.

In both cases where a plateau feature was seen in a microfield autocorrelation function, the plasma conditions gave $\xi_\nu Z_\nu > 1$ for ions dominating the field $\vec{F}_{ion}$ at the species of interest. As it also quantifies the condition just noted for some plateau-like behavior of the microfield distributions and their second moments, this simple inequality apparently provides a general rule of thumb for the appearance of τ-plateaus.

IV. AN IMPROVED MODEL FOR THE AVERAGING INTERVAL τ

It is unlikely that a τ-plateau can be identified from simulation data for high-Z – low-Z mixtures – using the field's autocorrelation function, a set of slow field distributions, or, its second moment behavior. Even when it can be done, there is considerable inconvenience (and computational expense) in relying on any of these *a posteriori* approaches. Therefore, in most instances we prefer to use a credible *a priori* model to estimate slow field averaging intervals.

The simple theoretical expression proposed in Paper I for calculating τ incorporates the constraint associated with the free-particle correlation timescales t_e and t_{ion}, but adds another constraint associated with properties of radiating electron bound states: To permit $\vec{F}_{slow}^{[\tau]}$ to be treated as a quasi-static perturbation, the averaging interval τ must exceed the minimum time needed to establish stationary radiator states. Our original expression for this timescale, t_{atom}, was based on a simple ion sphere model of plasma effects [37], and it did predict averaging intervals similar to those identified by a τ-plateau (when present). However, it contained no dependence on temperature or ion charge, and in high-Z – low-Z plasma mixtures these are important variables. The model developed below includes both of them.

Following Paper I, we adopt as a plausible minimum value for t_{atom} as the Bohr period of the circular orbit of the uppermost level, $n = n_{\max}$, remaining bound to a charge $Z_\nu e$ in the presence of plasma continuum lowering. This yields

$$t_{atom} \geq 3\pi\left(n_{\max}^3 / Z_\nu^2\right)\left(a_0 / \alpha c\right) \ , \tag{20}$$

where $(a_0 / \alpha c) = 2.42 \times 10^{-17}$ sec is the atomic unit of time. We now seek an approximation for $n_{\max}$ that is more realistic than the one used before. Our starting point is the well known Stewart-Pyatt (SP) treatment [38] of continuum lowering for an ion of nuclear (or core) charge $Z_\nu >> 1$ immersed in a hydrogen plasma. To obtain $n_{\max}$ for this ion, we assume, as is frequently done, that the plasma's reduction of its ionization potential (i.e., the lowering of its continuum) is by an amount $\Delta I_\nu(SP) > 0$ that simply truncates the original series of excited, hydrogenic excited states, whence

$$Z_\nu^2 I_H / n_{\max}^2 = \Delta I_\nu(SP) \ . \tag{21}$$

The Stewart-Pyatt model gives, by construction, the ion-sphere (IS) continuum lowering formula, $\Delta I_\nu(IS) = 3Z_\nu e^2 / 2a_\nu$, in the limit of strong electron-ion coupling, and the Debye-Huckel (DH) continuum lowering formula, $\Delta I_\nu(DH) = Z_\nu e^2 / D$, in the limit of weak electron-ion coupling. These simple expressions involve the radius a_ν of the charge-neutral ion sphere, determined by $4\pi a_\nu^3 N_e / 3 = Z_\nu$, and the Debye screening length D that incorporates all plasma species, viz., $D = D_e / \left(1 + Z_*\right)^{1/2}$, with $Z_* = \left[\left\langle Z^2 \right\rangle / \left\langle Z \right\rangle\right]$. By using

a_v to define a slightly different electron-ion coupling parameter, $\tilde{\Gamma}_{ev} = Z_v e^2 / a_v T$, the Stewart-Pyatt result can be written as

$$\Delta I_v(SP) = \Delta I_v(IS)\left\{\left[\left(\gamma_v^{3/2}+1\right)^{2/3}-1\right]/\gamma_v\right\} = \Delta I_v(IS)\; G(\gamma_v) \quad . \tag{22}$$

The second equality introduces a function $G(\gamma_v) \le 1$, whose argument is $\gamma_v = 3(Z_* + 1)\tilde{\Gamma}_{ev}$. The correct limiting form of ΔI_v for weak (strong) coupling is recovered when γ_v is much less (greater) than 1, and now $n_{\max}$ for the ionic core $Z_v e$ exhibits substantive temperature as well as density dependence whenever $\tilde{\Gamma}_{ev} < 1/3(Z_* + 1)$. Algebraic manipulation of Eqs. (20) - (22) enables the atomic timescale to be re-written in the convenient form

$$t_{atom} \ge \pi t_e / \left[G(\gamma_v)\right]^{3/2} \ge \pi t_e \quad , \tag{23}$$

which leads to the new inequality string $t_e < t_{atom} < \tau < t_{ion}$. Notice that, when electron coupling to all ions is strong and for each species $G(\gamma_v) \to 1$, all plasma ions have the same atomic timescale; in situations where electron-ion coupling is weak for some species, such as can easily happen in high-Z – low-Z mixtures, they have somewhat different atomic timescales.

Lacking more information, we still recommend that the geometric mean of the constraining limits be used to fix each species' averaging interval, viz., $\tau_v = \sqrt{t_{atom} \cdot t_{ion}}$. Then, the approximate ion timescale $t_{ion} \approx 60 t_e \left[\xi_e / \left(\xi_e + \xi_H\right)\right]^{1/2}$, together with Eq. (23), yields our default formula,

$$\omega_e \tau_v \approx 14 \left[\frac{\xi_e}{\xi_e + \xi_H}\right]^{1/4} \left[\frac{1}{G(\gamma_v)}\right]^{3/4} \quad . \tag{24}$$

In mixtures the first bracketed term always is somewhat less than unity, the second, always somewhat more, so this averaging interval is considerably larger than the interval needed to establish stationary electron screening of plasma ions, and a few times larger than the minimum interval needed to establish stationary radiator bound states. Under the conditions we consider, this τ_v limits the mean displacements of heavy ions, $Z_v \ge 6$, to a modest fraction of their ion-sphere radii a_v, but permits mean H^+ displacements of a few proton-sphere radii. An *ad hoc* reduction of ion dynamics effects could be achieved by replacing t_{ion}, as defined above for a mixture, by the relaxation time of the lightest ion species, but we have not yet studied the merits of this idea.

Table I contains the $\omega_e \tau_v$-value from Eq. (24) for the high-*Z* ion in each plasma simulated, and we used these values to check the QSP sensitivity of slow microfield distributions. We compared results for three plasmas, the cases C1, Ar2 and Kr4. Temperatures, densities, concentrations, and ion charges all vary, but differences in

$P_v(F_{slow}^{[\tau]})$ between simulations using the Dunn-Broyles and the Calisti-Talin QSPs are slight. On this important point, our conclusion of Paper I is reaffirmed for high-Z – low-Z mixtures.

V. COMPARISONS INVOLVING THE YUKAWA STATIC SCREENING MODEL

Even when the dynamical corrections in Eq. (5) are small for appropriate averaging interval(s) τ, the standard theory of Stark broadening can produce accurate line shapes only if the important correlations are accounted for. One-component plasma models treat the electrons as a uniform, charge-neutralizing background for the ions, thereby completely ignoring electron-electron and electron-ion correlations [39-41]. In Yukawa (ion-only) plasma models, electrons have a more realistic role as a source of localized, static screening; they are correlated individually with ions, but not with each other. The Yukawa fields are the correct static fields for the standard theory when electron-ion (and therefore electron-electron) interactions are weak; further, QSPs are unnecessary for Yukawa MD simulations, and there is no need to perform any short-time averaging. However, such simulations contain no dynamical information on electronic timescales, and cannot adapt the screening when plasma conditions move beyond the weak-coupling regime.

Here, we study statistical properties of plasma mixtures whose electrons are treated either implicitly with a Yukawa screening description, or explicitly with an all-particle description. With the goal of exploring limits for the validity of the simpler, Yukawa model, we make three kinds of comparisons – hypernetted chain (HNC) computations of pair distribution functions, MD simulations of (quasi-static) microfield probability distributions, and simulation-based determinations of the microfield second moments. To preview these results: Most mixtures show microfield distributions for F_{slow} and for F_{scr} at the high-Z ions that are in good agreement for the more probable field strengths. But, in cases where both Γ_{eZ} and the ratio Γ_{ZZ}/Γ_{eZ} are large, the Yukawa model significantly underestimates the plasma's screening of close high-Z pairs. This raises strong-field probabilities of the Yukawa microfields enough to cause a meaningful increase of their second moments.

A. Particle Distributions: All-particle HNC vs. Yukawa HNC

Because an MD simulation produces self-consistent particle and microfield distributions, pair distributions $g_{s's}(r)$ were used in Paper I to provide insight regarding certain features of the microfield distributions in C^{+6} – H^{+} plasmas. The pair distributions can be of similar value in the study of high-Z – low-Z mixtures, but we found that even 10^4 impurity ions do not provide very good statistics for the small values of $g_{s's}(r)$ of particular interest. Therefore, we employed a multi-species HNC code to determine pair functions for plasmas having ions and free electrons interacting via our standard QSPs (all-particle HNC), and for plasmas having Yukawa-screened ions (Yukawa HNC). It is known that such HNC calculations are in good agreement with results of MD simulations when both approaches employ the same potentials [8,24], and this has been confirmed for our code *ddcMD* [10,27].

HNC data in Fig. 9a pertain to hydrogen plasmas with 1% Kr^{+36} impurity ions. The total ion density is $N_{ion} = 10^{23} cm^{-3}$ or $10^{25} cm^{-3}$, and the temperature $T = 6.7\ keV$, near the lowest temperature at which our all-particle HNC algorithm converges for this plasma. Panel (a) shows sensitivity with respect to density of the pair distribution ratios

$\left\{ g_{Kr,v}[Yukawa] \div g_{Kr,v}[all\text{-}particle] \right\}$. When the plotted ratio is less than unity, it means that greater screening is produced by an all-particle treatment of electrons. (For these weakly coupled plasmas, $H^+ - H^+$ ratios have no meaningful departure from unity.) QSP effects on the all-particle results, important only very close to the origin, are not visible at the scale of these curves.

Figure 9b displays HNC results for the argon-argon pair distribution in $Ar^{+18} - H^+$ plasmas. As in our MD simulations for this mixture, the nucleon density is fixed, $N_{ion} = 10^{24} cm^{-3}$, while argon concentrations are varied, $\xi_{Ar} = 0.1,\ 0.01,\ 0.001$. However, instead of $1\ keV$, the temperature is $2.4\ keV$, which is close to the lowest value at which our HNC algorithm converges for these all-particle calculations. Even at this somewhat higher temperature, differences in the ratios $\left\{ g_{Ar,Ar}[Yukawa] \div g_{Ar,Ar}[all\text{-}particle] \right\}$ are substantial throughout an entire ion-sphere ($2.2 \le a_Z / a_0 \le 3.1$, depending on ξ_{Ar}). Additionally, the fact that each concentration's ratio lies below unity shows again that the effective interaction, i.e., the potential of mean force $U^{MF}_{Ar,Ar}(r)$, between a pair of Ar^{+18} ions in the all-particle system is smaller and has a shorter range than that of the Yukawa system. There also are screening effects on the Ar–H pair distributions, but in these plasmas the all-particle and Yukawa differences are slight.

In sum, these HNC calculations, and similar ones described in Paper I, reveal many-body screening of a given ion-ion interaction to be stronger when electrons are treated explicitly, and those screening differences to be greater when larger charges are involved.

B. Quasi-Static Microfield Distributions: All-particle MD vs. Yukawa MD

Below, we let F and β without additional specification denote either the slow field quantities of all-particle MD, or the static-screened quantities of Yukawa MD.

The first set of distribution comparisons for low-Z – high-Z mixtures involves the hydrogen plasmas with Kr^{+36} impurities. Temperature, impurity concentration,and the ion densities are as listed in Table I for cases Kr1,Kr2 and Kr3; the largest ion density gives an electron-Kr coupling constant of only $\Gamma_{e,Kr} = 0.2$. Each of the top panels of Fig. 10 places the Yukawa distribution among slow field distributions $P_{Kr}(\beta^{[\tau]}_{slow})$, for three averaging intervals that include a value near the $\omega_e \tau$ given by Eq. (24). The results show that the Yukawa microfield distributions for the lower two densities are close to the slow field distribution for the recommended τ-value. However, at the highest plasma density, inspection shows that there actually is better agreement, at large β-values, with a smaller τ-value's distribution having higher probability densities there. All of these low-$\Gamma_{e,Kr}$ distributions differ considerably from their (all-particle) Holtsmark counterparts.

The bottom panels of Fig. 10 compare MD distributions at Ar^{+18}, in the three argon-hydrogen mixtures presented in Figs. 4 and 5 (cases Ar1,Ar2,Ar3). Even as the argon concentration increases a hundredfold, and $\Gamma_{e,Ar}$ rises from 0.4 to 0.6, we see little difference between the Yukawa and the all-particle results throughout the range of β-values for which $P_{Ar}(\beta) \ge 0.1$. The same can be said about the probability distributions at H^+ ions in these

plasmas. Another point shown by Fig. 10 is how higher ξ_{Ar}-values and, hence, higher electron densities and greater screening, cause larger differences between the distribution $P_{Ar}(\beta_{ion})$ due to fields of unscreened ions and that due to fields of either screened-ion picture.

These results suggest that Yukawa simulations (MD or Monte Carlo) can yield reliable microfield distributions in high-Z – low-Z mixtures even when $\Gamma_{ev} \approx \frac{1}{2}$. To pursue the question of when Yukawa screening fails to adequately characterize plasma correlations, we carried out two more pairs of MD simulations (all-particle and Yukawa) for plasmas with even larger argon concentration, $\xi_{Ar} = \frac{1}{3}$. In one pair the temperature remains $T = 1\ keV$, and in the other, it is $T = 3\ keV$; the coupling constants $\Gamma_{e,Ar}$ for these plasmas are 0.80 and 0.27. Figure 11 places the Yukawa MD results for these mixtures among corresponding slow field distributions obtained for a few averaging intervals. Panel (a) results for the higher temperature (and smaller $\Gamma_{e,Ar}$-value) plasma show good over-all agreement at $\omega_e\tau = 17$, which is close to the averaging interval specified by Eq. (24). However, panel (b) shows that, except very near its peak, the 1 *keV* Yukawa distribution agrees with the slow-field distribution obtained for the unreasonable value $\omega_e\tau = 93$ (i.e., $\tau > t_{ion}$). Here, at last, is a substantive breakdown of the Yukawa model for low-frequency microfields. Such a failure is not surprising, in and of itself, but the fact that it requires a Γ_{eZ}-value approaching unity is.

Of course, additional phenomena could be involved in this breakdown, and an obvious possibility is strong correlations among the high-Z impurities. Pair distribution ratios plotted in Fig. 9 offer some insight into the consequences of ion-ion correlation differences arising from the alternative versions of electron screening. For example, the HNC data for $N_{ion} = 10^{25} cm^{-3}$ indicate that Yukawa screening results in fewer very close krypton-krypton pairs than does all-particle (i.e., free electron) screening; that weaker screening leads to quasi-static Yukawa fields whose probabilities at large β-values are slightly higher. This trend, which was noted above for one hydrogen-krypton mixture, is hard to see at the scale of Fig. 10. More apparent, and to be discussed below, are the consequences of ion-ion correlations for second moments of the distributions.

In hydrogen plasma with a single impurity species Z, the ratio Γ_{ZZ}/Γ_{eZ} of our coupling constants, defined in Eq. (9), is largest when $Z\xi_Z >> 1$, for in that situation

$$\Gamma_{ZZ}/\Gamma_{eZ} = Z^{2/3}\left[Z\xi_Z/\left(1+Z\xi_Z\right)\right]^{1/3} \to Z^{2/3} \qquad . \tag{25}$$

The argon-hydrogen plasma whose microfield distributions are plotted in Fig. 11b has the largest value of both $\Gamma_{e,Ar}$ and the above ratio. Further, the decomposition data of Fig. 4 show the dominating role other Ar^{+18} ions have on $\vec{\beta}_{ion}$ when $\xi_{Ar} \geq 0.1$. Together, these conditions indicate a sensitivity of $P_{Ar}(\beta)$ to the ion-ion correlation differences. Additional evidence for the influence of this other factor in our simulations involves carbon-hydrogen mixtures studied in Paper I. There, we reported all-particle and Yukawa MD distributions for quasi-static microfields in plasmas with ion density $N_{ion} = 10^{23} cm^{-3}$, C^{+6} abundances of 0.01 and 2/3, and three different temperatures. We saw disagreement only at the lowest

temperature and highest carbon concentration -- the mixture of these elements that had the largest values of Γ_{eC} *and* Γ_{CC}/Γ_{eC}.

Now, recall that $Z\xi_Z > 1$ was a necessary condition for plateau-like behavior in the microfield autocorrelation function for either component of an H^+–high-Z mixture. Once we connect this with the fact that $\Gamma_{eZ} \propto (1+Z\xi_Z)^{1/3}$, we see that an $A(t)$ plateau feature is not likely unless Γ_{eZ} is large enough for the Yukawa form of electron screening to have failed.

C. Mean Squared Microfields: All-particle MD vs. Yukawa MD

Ostensibly, these are the simplest comparisons to make because they involve just single numbers. Each Yukawa distribution gives a unique value of $\langle\beta^2\rangle$, but as we found in Sec. III.C, there is a gradual decline as a function of averaging interval τ in the slow field's second moment $\langle\beta^2(\tau)\rangle$. This leads to agreement of these two distributions' second moments at some τ-value. For a meaningful comparison we must first set bounds on τ, and then use that limited range of τ-values to identify credible slow-field values of $\langle\beta^2(\tau)\rangle$. All the second moments we discuss here are determined directly as ensemble averages, not as integrals involving fitted probability distributions.

Figure 12 contain sets of curves showing $\langle\beta^2(\tau)\rangle_\nu$ vs. averaging interval over three decades, $0.1 \le \omega_e\tau_\nu \le 100$, for hydrogen plasmas with different conditions and different impurity ions; open circles in each panel mark intersections with $\langle\beta^2\rangle_\nu$ given by the corresponding Yukawa MD simulations. According to Table I, for impurity ions in the plasmas we simulated, values of $\omega_e\tau_\nu$ given by Eq. (24) range from 13 to 23. The plotted data show that varying $\omega_e\tau_\nu$ between 10 and 25 (the shaded vertical strips) results in no more than a $\pm 10\%$ change in the value of $\langle\beta^2(\tau)\rangle_\nu$ for any of those cases.

For hydrogen plasmas with C^{+6} impurities there is good agreement, at all three densities, between the second moments obtained from the all-particle and the Yukawa MD simulations. However, this is not so for the plasmas with Kr^{+36} impurities: the τ-value for which the slow field's second moment equals the second moment of the Yukawa MD fields becomes unrealistically small (less than the electron relaxation timescale) at the higher total ion densities. Moreover, they are not close to the τ-values one identifies in Fig. 10 as giving slow-field distributions in good overall agreement with the Yukawa distributions. The explanation of this disparity lies with the aforementioned strong-field probability differences generated by the two simulation models. Consider the case with $N_{ion} = 10^{25} cm^{-3}$, for which only Kr^{+36} – Kr^{+36} correlations would be important. A conclusion from information displayed in Fig. 2 and Fig. 9a is that Yukawa MD persistently overestimates the plasma's (small) microfield probabilities when $\beta \ge 15$, by enough to raise its second moment well above any likely value of $\langle\beta^2(\tau)\rangle_{Kr}$. This same behavior occurs at the lower densities but is less marked there. However, even with this explanation, we are left with the question of

why the C and the Kr comparisons of $\langle \beta^2 \rangle_\nu$ have such different results, when ion density and impurity concentration match and $\langle Z \rangle$ and ion-ion coupling constants are similar in both sets of mixtures. We believe the cause of these differences is that the disparity, at small r-values, between Yukawa and all-particle effective pair interactions (and, hence, effective single-ion fields) grows with increasing Z_ν.

The argon data in Fig. 12c exhibit the trend noted in Section III.C, namely, that individual $\langle \beta^2(\tau) \rangle$ curves for smaller impurity concentrations in H^+ plasmas have larger slopes in the interval between t_e and t_{ion} (a signature of ion motion effects). We expect Yukawa MD to overestimate $\langle \beta^2 \rangle_{Ar}$ for the large argon concentrations, as happens in the krypton results of panel (b) and in these argon results at the intermediate ξ_{Ar}-values. However, the overall systematic change with ξ_{Ar} in the τ-values for which the second moments match is not present, and the other two argon cases seem anomalous: In the plasma with $\xi_{Ar} = 0.001$ the Yukawa value of $\langle \beta^2 \rangle_{Ar}$ agrees with the all-particle second moment of a slow field distribution for a much shorter than expected averaging interval, $\omega_e \tau \approx 3$, while in the plasma with $\xi_{Ar} = \frac{1}{3}$ the Yukawa value of $\langle \beta^2 \rangle_{Ar}$ agrees with the all-particle second moment of a slow field distribution for a much longer than expected averaging interval, $\omega_e \tau \approx 30$.

Some details for these two cases are revealed in Fig. 13, where we have plotted their cumulative moment quantities,

$$Q_{Ar}^{[\lambda]}(\beta) = \int_0^\beta dx\, x^\lambda P_{Ar}(x) \ , \tag{26}$$

for $\lambda = 0, 2$. Being determined directly from the simulation data, each of these "curves" actually is composed of 10^4 points representing ordered sums. Panel (a) and the blow-up of its upper portion, panel (b), show that, beyond the peak of the probability distribution (at $\beta \approx 3$), the Yukawa result for $\xi_{Ar} = \frac{1}{3}$ begins to shift away from the slow field distribution of all-particle MD for $\omega_e \tau = 93$, and toward the larger values of the slow field distribution for $\omega_e \tau = 16$. This behavior results from differences in the complicated interplay of greater screening (more free electrons) and more nearby high-Z ions, as determined by the all-particle and Yukawa models. Panel (c) shows the combined effects of these features on the numerical development of the second moment.

The mixture with the smallest Ar^{+18} impurity concentration, $\xi_{Ar} = 0.001$, has weak enough correlations that there is general agreement between microfield distributions for the two screening models at the expected value of $\omega_e \tau$ (see Fig. 10). However, details for this case, shown in the lower panels of Fig. (13), reveal a shift – beginning well beyond the distribution's peak at $\beta \approx 1$ – of the Yukawa result away from that of the slow field for $\omega_e \tau = 16$ and toward the larger probability densities of the slow field for $\omega_e \tau = 2.9$. It is puzzling why this case has such a large *relative* disparity between the second moments. This

is not a small-number statistics problem, as there are 10^4 impurity ions in this simulation, too. Also, there are very small differences between the Yukawa and all-particle HNC distributions for the (Ar^{+18}, H^+) pairs that dominate fields at Ar ions in this particular plasma. Perhaps non-stationary effects of close electrons are still influencing $F_{slow}^{[\tau]}$ at $\omega_e\tau = 2.9$. Further analysis is needed to clarify this detail.

To conclude the discussion, we recall that $Z\xi_Z > 1$ was a necessary condition for plateau-like behavior in the microfield autocorrelation function for either component of an H–high-Z mixture. Once we connect this with the fact that $\Gamma_{eZ} \propto (1 + Z\xi_Z)^{1/3}$, we see that an $A(t)$ plateau feature is not likely unless Γ_{eZ} is large enough for the Yukawa form of electron screening to have failed. The same statement can be made regarding plateau behavior by the second moment quantity $\left\langle \beta_{slow}^2(\tau) \right\rangle$.

VI. SUMMARY AND OUTLOOK

This work investigated dynamical and stationary properties of microfields at large impurity charges in hydrogen plasmas whose conditions can be achieved at many high energy density facilities. Diagnostic measurements for these high-Z – low-Z mixtures often include spectral line intensities and shapes. The "standard theory" of line broadening uses static microfields to determine Stark effects on radiating ions. Usually these microfields $\vec{F}_{scr}$ are taken to be the net result of electron-screened fields of stationary ions, with the screening having the Yukawa form for weak electron-ion coupling. By using large-scale MD that includes ions *and* electrons (here called all-particle MD), it is possible to explore microfield properties at all relevant plasma timescales and coupling strengths in the classical regime.

We first studied statistical properties of the total field $\vec{F}_{tot}(t)$ experienced by different ions. We used classical dynamics with quantum statistical potentials to obtain the stationary probability distributions of $\vec{F}_{tot}$ and of its contributing species, as well as the autocorrelation function for $\vec{F}_{tot}(t)$, all for a variety of H^+ plasmas with free electrons and C^{+6}, Ar^{+18}, or Kr^{+36} impurities. We then addressed the first of two key questions: How is the *quasi-static* field $\vec{F}_{slow}$ that is approximated by $\vec{F}_{scr}$ to be extracted from the time-dependent total field of all-particle MD? We followed earlier researchers [6,7,10] and determined this slow field from a running, short time (τ) average of $\vec{F}_{tot}(t)$ at each ion. We devoted considerable attention to the issue of the best choice for τ. Our favored scheme involves free-particle relaxation times and an atomic timescale constraint related to the requirement of stationary radiator states in the presence of plasma continuum lowering. The simulations discussed in Sec. III also reveal electron and proton dynamical timescales to be close enough that, when protons dominate the total ionic field at a given species, any appropriate averaging interval τ for the field $\vec{F}_{slow}^{[\tau]}$ defined in Eq. (5) produces noticeable ion-motion effects on its statistical properties.

Next, we turned to the second key question: What are the plasma conditions for which fields of the simpler Yukawa model become unreliable? For this, we made several

comparisons of properties of quasi-static microfields obtained from analogous all-particle and Yukawa MD simulations, and these were augmented by comparisons of particle distribution functions obtained from all-particle and Yukawa HNC calculations. In the majority of plasmas considered, the probability distributions for F_{slow} and for F_{scr} were in good overall agreement. But, when strong Coulomb coupling exists between high-Z ion pairs *and* between (electron, high-Z) pairs, we found that the Yukawa model underestimates the plasma's screening of close high-Z pairs. This leads to Yukawa microfield distributions having somewhat higher strong-field probabilities. The differences affect only the far wings of spectral lines, and do not directly impact most plasma diagnostics. However, they can noticeably alter a distribution's second moment $\left\langle F^2 \right\rangle$. This is a result with potentially important consequences for the well-known APEX microfield method [42-44], which relies on accurate second moments to fix an essential parameter. Work on this topic is underway and will be reported elsewhere.

Looking further ahead, we plan to incorporate the quasi-static Stark effects of $\vec{F}_{slow}$ into our "Small Ball" model [11,27] of atomic processes for MD simulations as a *localized* source of continuum lowering, in much the same way as Hummer and Mihalas [45] used the distribution of Holtsmark fields.

Our last comment concerns ion dynamics, whose importance in shaping the central regions of hydrogenic emission lines was an unexpected experimental discovery [4]. Most efforts to treat the observed, strong dependence on perturber ion masses involve some extension of the standard theory, specifically, the new dynamical effects of the radiator-(ion microfield) interaction still are treated separately from the dynamical (i.e., collisional) effects of interactions with plasma electrons [46-50]. All-particle MD is ideally suited to an alternative, unified line-shape prescription in which the field history $\vec{F}_{tot}(t)$ at each member of an ensemble of electric-dipole radiators is input to a quantum solver for that dipole's time-dependence. The complete line profile is then computed directly from the Fourier transform of the ensemble's dipole autocorrelation function [4,5]. Some realistic results using this approach have been reported [e.g., 21,51, and references therein], and large sets of time histories such as we have produced can advance this promising research front.

ACKNOWLEDGMENTS

We thank Drs. C. A. Iglesias and J. W. Dufty for very useful comments regarding a preliminary version of this work, and Dr. F. R. Graziani for his continuing interest and support. Our research was performed under the auspices of the U.S. Department of Energy by Lawrence Livermore National Laboratory under Contract DE-AC52-07NA27344.

REFERENCES

[1] J. Holtsmark, Ann. Physik **58**, 577 (1919).

[2] S. Chandrasekhar, Rev. Mod. Phys. **15**, 1 (1943).

[3] A.V. Demura, Int. J. Spectrosc. **2010**, 671073 (2010).

[4] H.R. Griem, *Principles of Plasma Spectroscopy* (Cambridge U. Press, Cambridge, 1997).

[5] D. Salzmann, "*Atomic Physics in Hot Plasmas*," (Oxford U. Press, Oxford, 1998).

[6] A. Calisti, B. Talin, S. Ferri, C. Mosse, V. Lisitsa, L. Bureyeva, M.A. Gigosos, M.A. gonzalez, T del Rio Gaztelurrutia and J.W. Dufty, in *Spectral Line Shapes, Vol. 19*, Proceedings of the 19th International conference on spectral Line shapes, AIP Conf. Proc. No. 1058, ed. M.A. Gogosos and M.A. Gonzalez (AIP, New York, 2008).

[7] A. Calisti, S. Ferri, C. Mosse, B. Talin, M.A. Gigosos, and M.A. Gonzalez, High Energy Density Phys. **7**, 197 (2011).

[8] H.B. Nersisyan, C. Toepffer, and G. Zwicknagel, Phys. Rev. E **72**, 036403 (2005).

[9] S.P. Sadykova, W. Ebeling, I.M. Sokolov, and I.A. Valuev, Plasma Phys. Reports **36**, 1161 (2010).

[10] S. Hau-Riege and J. Weisheit, Phys. Rev. E **91**, 033106 (2015).

[11] F.R. Graziani, V.S. Batista, L.X. Benedict, J.I. Castor, H. Chen, S.N. Chen, C.A. Fichtl, J.N. Glosli, P.E. Graboski, A.T. Graf, S.P. Hau-Riege, A. U. Hazi, D.F. Richards, H.A. Scott, R. Shepherd, L.G. Stanton, F.H. Streitz, M.P. Surh, J.C. Weisheit, and H.D. Whitley, High Energy Density Phys. **8**, 105 (2012).

[12] T. R. Boehly, R. S. Craxton, T. H. Hinterman, J. H. Kelly, T. J. Kessler, S. A. Kumpan, S. A. Letzring, R. L. McCrory, S. F. B. Morse, W. Seka, S. Skupsky, J. M. Soures, and C. P. Verdon, Rev. Sci. Instrum. **66**, 508 (1995).

[13] G. H. Miller, E. I. Moses, and C. R. Wuest, Opt. Eng. **43**, 2841 (2004).

[14] B. Nagler, B. Arnold, G. Bouchard, R. F. Boyce, R. M. Boyce, A. Callen, M. Campell, R. Curiel, E. Galtier, J. Garofoli, E. Granados, J. Hastings, G. Hays, P. Heimann, R. W. Lee, D. Milathianaki, L. Plummer, A. Schropp, A. Wallace, M. Welch, W. White, Z. Xing, J.Yin, J. Young, U. Zastrau and H. J.Lee, J. Synchr. Rad. **22**, 520 (2015).

[15] J.-P. Hansen and I.R. McDonald, "*Theory of Simple Liquids*," 3ed. (Academic Press, Amsterdam, 2006). This monograph contains a comprehensive discussion of time-dependent correlation phenomena in dense matter in Chapt. 7 – 9.

[16] M.A. Berkovsky, J.W. Dufty, A. Calisti, R.Stamm, and B. Talin, Phys. Rev. **E54**, 4087 (1996).

[17] M.T. Meftah, T. Chorah, H. Bouguettaia, F. Khelfaoui, B. Talin, A. Calisti, and J.W. Dufty, Eur. Phys. J. **B37**, 39 (2004).

[18] B. Talin, A. Calisti, J.W. Dufty and I.V. Pogorelov, Phys. Rev. **E77**, 036410 (2008).

[19] M. Baranger and B. Mozer, Phys. Rev. **115**, 521 (1959); **118**, 626 (1960).

[20] S. Alexiou, High Energy Density Phys. **5**, 225 (2009).

[21] E. Stambulchik and Y. Maron, High Energy Density Phys. **6**, 9 (2010).

[22] C. Iglesias and J. Dufty, in *Spectral Line Shapes*, ed. K. Burnett (W. de Gruyter, Berlin, 1983) Vol. II, p55.

[23] C.F. Hooper, Jr, Phys. Rev. **149**,77 (1966); **165**, 215 (1968).

[24] J.-P. Hansen and I.R. McDonald, Phys. Rev. A **23**, 2041 (1981).

[25] C.S. Jones and M.S. Murillo, High Energy Density Phys. **3**, 379 (2007).

[26] L.X. Benedict, M.P. Surh, J.I. Castor, S.A. Khairallah, H.d. Whitley, D.R. Richards, G.N. Glosli, M.S. Murillo, C.R. Scullard, P.E. Graboski, D. Michta, and F.R. Graziani, Phys. Rev. E **86**, 046406 (2012).

[27] S.P. Hau-Riege, J. Weisheit, J.I. Castor, R.A. London, H. Scott, and D.F. Richards, New J. Phy. **15**, 015011 (2013).

[28] P.E. Grabowski, M.P. Surh, D.F. Richards, F.R. Graziani, and M.S. Murillo, Phys. Rev. Lett. **111**, 215002 (2013).

[29] H.D. Whitley, Ch. R. Scullard, L.X. Benedict, J.I. Castor, A. Randles, J.N. Glosli, D.F. Richards, M.P. Desjarlais, and F.R. Graziani, Contrib. Plasma Phys. **55**, 192 (2015).

[30] T. Dunn and A.A. Broyles, Phys. Rev. **157**,156 (1967).

[31] F. Lado, J. Chem. Phys. **47**, 5369 (1967).

[32] A. Calisti, T. del Rio Gaztellutitia, and B. Talin, High Energy Density Phys. **3**, 52 (2007).

[33] A. Calisti and B. Talin, Contrib. Plasma Phys. **51**, 524 (2011).

[34] B.J.B. Crowley, High Energy Density Phys. **13**, 84 (2014).

[35] E.Stambulchik, D.V. Fisher, Y. Maron, H.R. Griem, and S. Alexiou, *High Energy Density Phys.* **3**, 272 (2007).

[36] J.P. Boon and S. Yip, "*Molecular Hydrodynamics*," Chapt. 3 (Dover Publ., Mineola, N.Y., 2013).

[37] R.M. More , in *Advances in Atomic and Molecular Physics*, Vol. 21, ed. D.R. Bates and B. Bederson (Academic Press, Orlando, FL, 1984).

[38] J.C. Stewart and K.D. Pyatt, Astrophys. J. **144**, 1203 (1966).

[39] M. Baus and J.P. Hansen, Phys. Reports **59**, 1 (1980).

[40] E.L. Pollock and J.C. Weisheit, in *Spectral Line Shapes*, ed. F. Rostas (W. de Gruyter, Berlin, 1985) Vol. III, p181.

[41] J.W. Dufty, D.B. Boercker and C.A. Iglesias, Phys. Rev. **A31**, 1681 (1985).

[42] C.A. Iglesias, J.L. Lebowitz, and D. MacGowan, Phys. Rev. A **28**, 1667 (1983).

[43] C.A. Iglesias, H.E. DeWitt, J.L. Lebowitz, D. MacGowan, and W.B. Hubbard, Phys. Rev. A **31**, 1698 (1985).

[44] C.A. Iglesias, F.J. Rogers, R. Shepherd, A. Bar-Shalom, M.S. Murillo, D.P. Kilcrease, A. Calisti, and R.W. Lee, J. Quant. Spectrosc. Radiat. Transfer **65**, 303 (2000).

[45] D.G. Hummer and D. Mihalas, Astrophys. J. 331, 794 (1988).

[46] U. Frisch and A. Brissaud, J. Quant. Spectrosc. Radiat. Transfer **11**, 1753 (1971); 1767 (1971).

[47] R. Stamm and D. Voslamber, J. Quant. Spectrosc. Radiat. Transfer, **22**, 599 (1979).

[48] R. Stamm, B. Talin, E.L. Pollock and C.A. Iglesias, Phys. Rev. A34, 4144 (1986).

[49] D.B. Boercker, C.A. Iglesias and J.W. Dufty, Phys. Rev. **A36**, 2254 (1987).

[50] S. Ferri, A. Calisti, C. Mosse, J. Rosato, B. Talin, S. Alexiou, M.A. Gigosos, M.A. Gonzalez, D. Gonzalez-Herrero, N. Lara, T. Gomez, C. Iglesias, S. Lorenzen, R.C. Mancini, and E. Stambulchik, Atoms **2**, 299 (2014).

[51] H.B. Nersisyan, C. Toepffer, and G. Zwicknagel, Contrib. Plasma Phys. **50**, 193 (2010).

CAPTION FOR TABLE

Table I. Physical parameters for simulations discussed in the text. The first column assigns each simulation case a short label we use for easy reference.

CAPTIONS FOR FIGURES

Figure 1. Scaled probability distributions $P_{Kr}(\beta_{tot})$ and $P_H(\beta_{tot})$ at Kr^{+36} and at H^+ in plasmas. Panels (a) and (d), (b) and (e), and (c) and (f) correspond to simulation cases Kr1, Kr3, and Kr4, respectively. [CT] denotes the result when the QSP of Eq. (12) is used. The corresponding Holtsmark distribution, Eq. (15), is plotted for each case. The scaled microfield is $\beta_{tot} = F_{tot} / F_0$, and F_0 is the atomic unit of field strength.

Figure 2. Scaled probability distributions $P_{Kr}(\beta_x)$ and $P_H(\beta_x)$ for the total microfield, and for its respective component species, at Kr^{+36} and at H^+ ions, for simulation case Kr3. Each arrow indicates the ordering of curves corresponding to that panel's legend: top label belongs to first curve intersected, etc.

Figure 3. Scaled probability distributions $P_{Ar}(\beta_x)$ and $P_H(\beta_x)$ for the total microfield at Ar^{+18} and at H^+ ions. The label [CT] is defined as in Fig. 1, and the arrows, as in Fig. 2.

Figure 4. Scaled probability distributions $P_{Ar}(\beta_x)$ and $P_H(\beta_x)$ for the total microfield, and for its respective component species, at Ar^{+18} and at H^+ ions. Panels (a) and (d), (b) and (e), and (c) and (f) correspond to simulation cases Ar1, Ar2, and Ar3, respectively. Arrows connect the ordering of the curves and the legend.

Figure 5. Scaled probability distributions of the slow microfield for different values of the dimensionless interval parameter $\omega_e \tau$. Panels (a), (b) and (c) correspond to the simulation cases C1, Ar3, and Kr2, respectively. Arrows connect the ordering of the curves and the legend.

Figure 6. Autocorrelation functions $A_\nu(t)$ of the total field at various ions ν, for different plasma conditions. Arrows connect the ordering of the curves and the legend.

Figure 7. Scaled second moment of the slow microfield as a function of the dimensionless interval parameter $\omega_e \tau$, for high-Z ions. Dots mark parameter values of Table I, and the arrow connects the ordering of the curves and the legend. The dashed curve marked [h] Kr3 denotes results when H^+ ions are given a mass equal to that of krypton.

Figure 8. Properties of scaled slow microfields at Kr^{+36} ions, for simulation case [h] Kr3 in a plasma of H^+ ions whose mass equals that of krypton. Arrows connect the ordering of the curves and the legend's values of $\omega_e \tau$.

Figure 9. Ratios of ion-ion pair distribution functions $g_{ss'}(r)$ as determined by Yukawa HNC and all-particle HNC. Panel (a): krypton-hydrogen plasmas with $\xi_{Kr} = 0.01$, T=6.7

keV and two different ion densities; panel (b) argon-hydrogen plasmas with $N_{ion} = 10^{24} cm^{-3}$, T=2.4 keV, and three different argon concentrations. Arrows connect the ordering of the curves and the legend.

Figure 10 Top row: comparisons of small sets of scaled slow field probability distributions at Kr^{+36} with Yukawa MD and Holtsmark results, for (left to right) simulation cases Kr1,Kr2, Kr3. Bottom row: comparison of probability distributions at Ar^{+18}, for (left to right) simulation cases Ar1, Ar2, and Ar3. Shown here are the slow field and the field of plasma ions only, both for all-particle MD, and the Yukawa MD result. Arrows connect the ordering of the curves and the legend.

Figure 11. Scaled probability distributions of the slow microfield for different values of the interval parameter $\omega_e \tau$ are compared with Yukawa MD results, in mixtures with high Ar^{+18} concentration, $\xi_{Ar} = \frac{1}{3}$. Panels (a) and (b) show near-peak values for simulation cases Ar5 and Ar4, respectively. Arrows connect the ordering of the curves and the legend.

Figure 12. Scaled second moments of the slow microfield, plotted as in Fig. (7), are compared with the corresponding fixed values calculated from Yukawa MD (horizontal dashed lines). Dots mark curve intersection points, and shaded bars denote the range of plausible $\omega_e \tau$ -values. Panel (a): at C^{+6} impurities. Panel (b): at Kr^{+36} impurities. Panel (c): at Ar^{+18} impurities. Each panel's order of its curves is the same as the legend.

Figure 13. Comparisons of cumulative microfield distribution moments, $Q_{Ar}^{[\lambda]}(\beta)$, $\lambda = 0$ or $\lambda = 2$, for Yukawa and all-particle screening models in selected argon-hydrogen mixtures: simulation case Ar4 for panels (a) to (c), and simulation case Ar1 for panels (d) to (f). Panels (b) and (e) show upper end of data in panels (a) and (d), respectively, on a much expanded scale. Arrows connect the ordering of the curves and the legend.

Name	plasma	ξ_v	T	N_{ion}	<Z>	Z_{mix}	D_e	e^2/aT	Γ_{ev}	Γ_{vv}	ω_e	$\omega_e\tau_v$
	(H^+/v)		(keV)	(10^{24} cm^{-3})			(a_0)				(1/fs)	
C1	H^+/C^{+6}	1	0.2	0.1	6.00	2.06	2.60	0.054	0.62	1.94	43.7	15.3
C2		0.01	0.2	0.1	1.05	1.04	6.20	0.054	0.33	0.42	18.3	16.7
C3		0.01	0.2	1.0	1.05	1.04	1.96	0.116	0.71	0.90	57.8	14.4
C4		0.01	0.2	10.0	1.05	1.04	0.62	0.250	1.53	1.94	182.8	13.1
Ar1	H^+/Ar^{+18}	0.001	1	1.0	1.02	1.02	4.46	0.023	0.42	0.75	56.9	17.1
Ar2		0.01	1	1.0	1.17	1.22	4.16	0.023	0.44	1.62	61.0	14.9
Ar3		0.1	1	1.0	2.70	2.10	2.74	0.023	0.59	3.49	92.7	14.0
Ar4		0.33	1	1.0	6.67	2.63	1.74	0.023	0.80	5.22	145.7	14.2
Ar5		0.33	3	1.0	6.67	2.63	3.02	0.008	0.27	1.74	145.7	15.3
Kr1	H^+/Kr^{+36}	0.01	10	0.1	1.35	1.54	38.69	0.001	0.04	0.30	20.7	23.2
Kr2		0.01	10	1.0	1.35	1.54	12.23	0.002	0.09	0.65	65.6	18.4
Kr3		0.01	10	10.0	1.35	1.54	3.87	0.005	0.20	1.40	207.3	15.5
Kr4		0.01	5	10.0	1.35	1.54	2.74	0.010	0.40	2.79	207.3	14.0

Table I

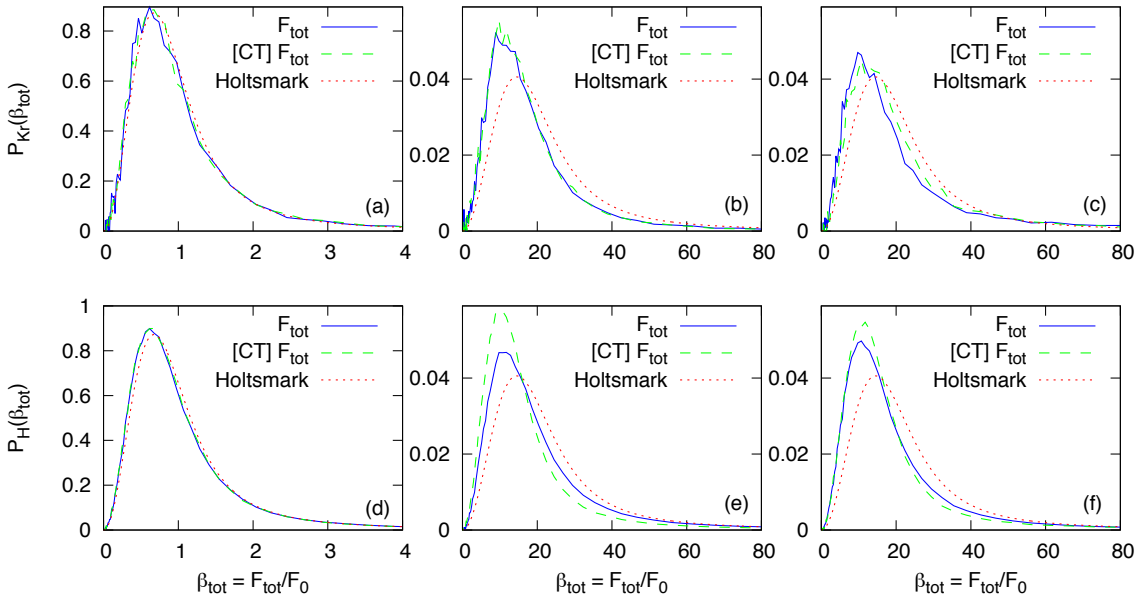

Figure 1

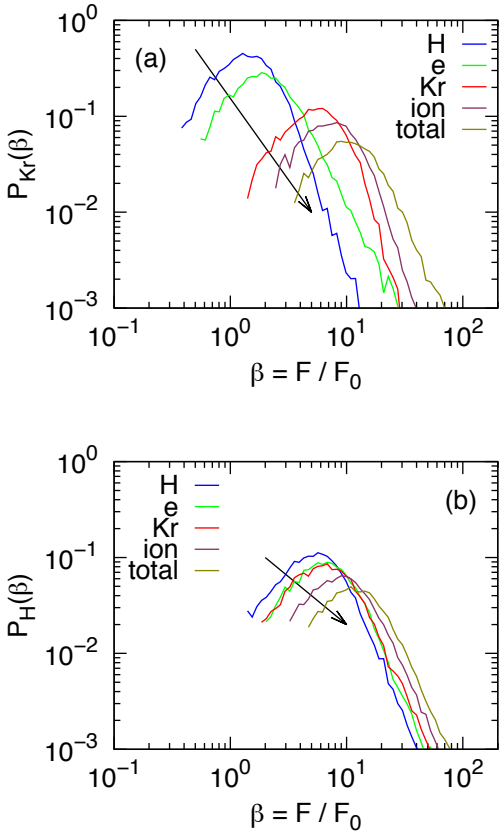

Figure 2

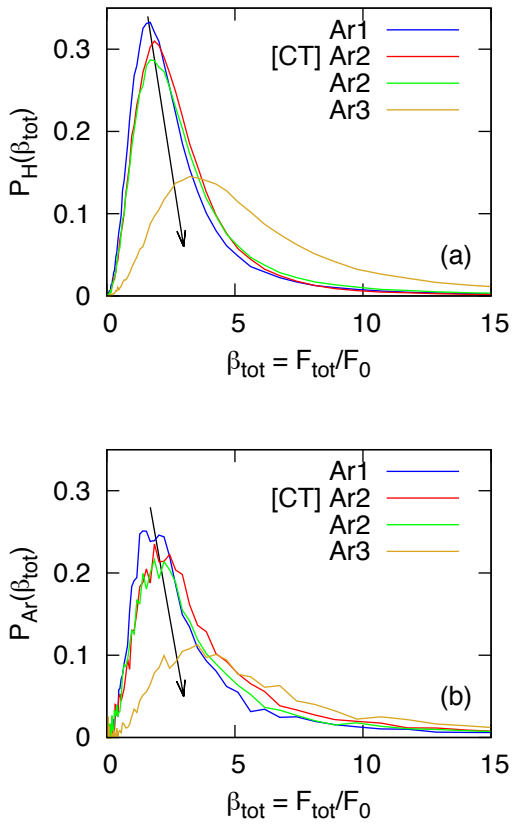

Figure 3

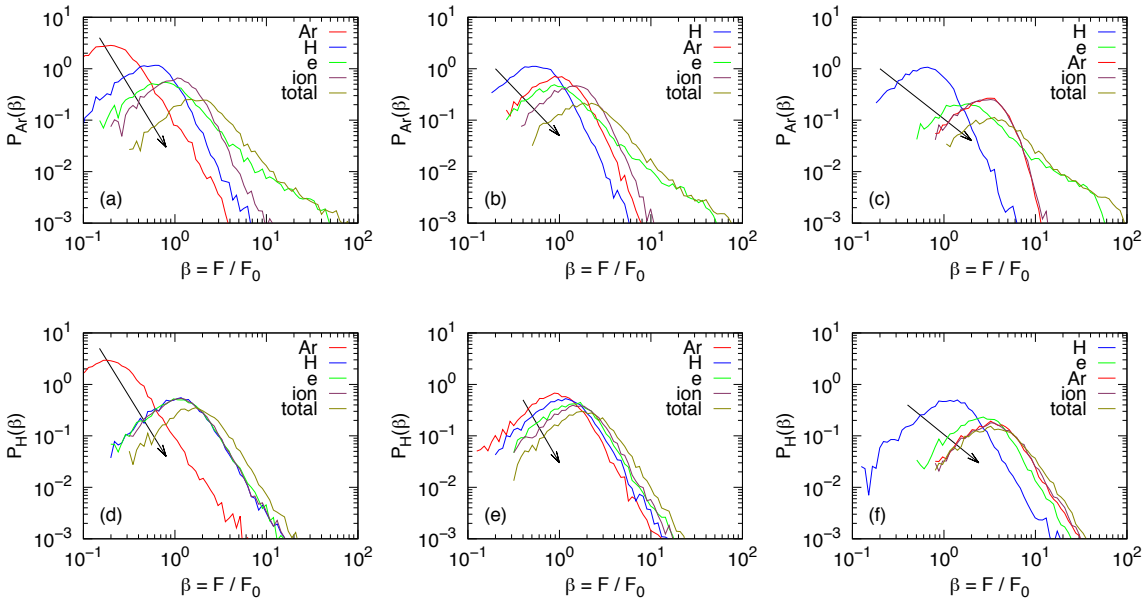

Figure 4

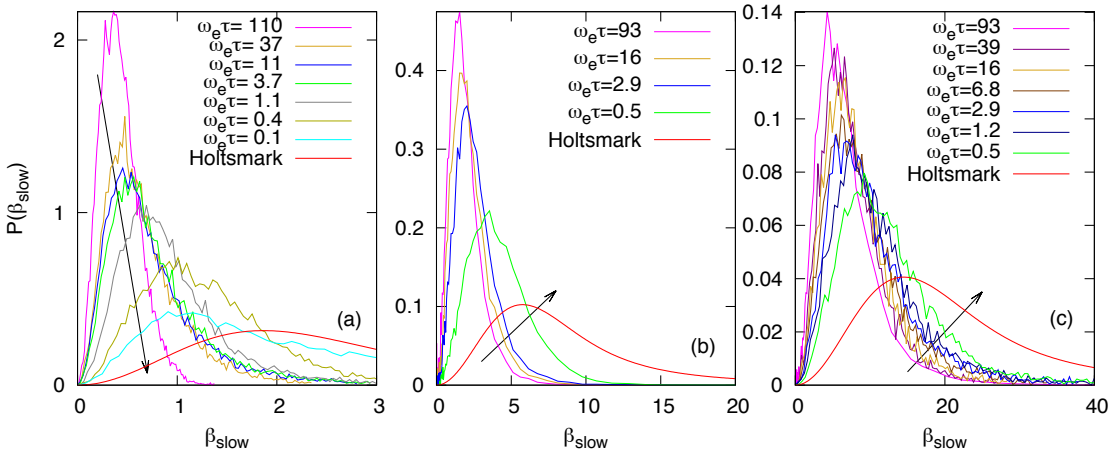

Figure 5

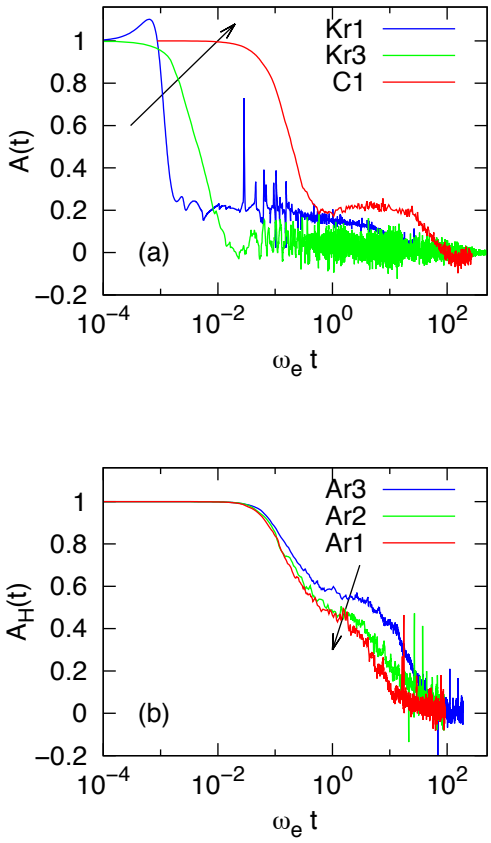

Figure 6

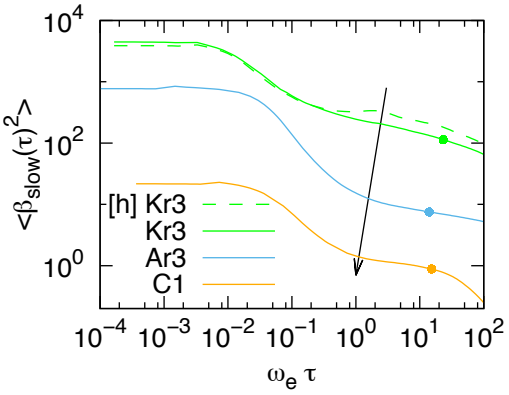

Figure 7

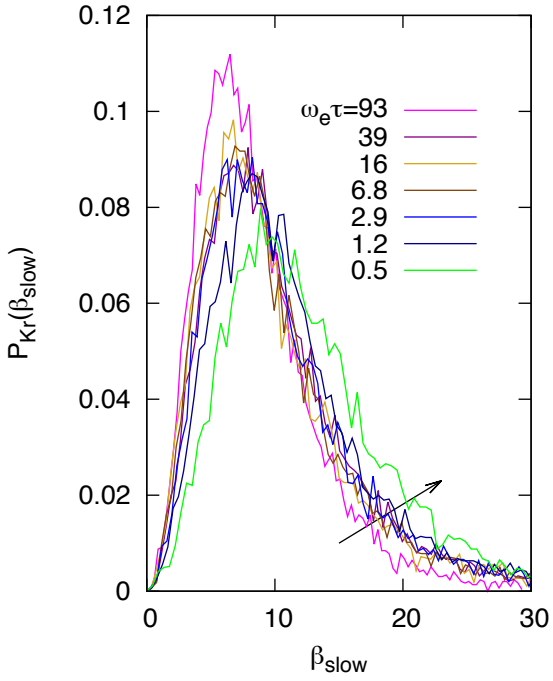

Figure 8

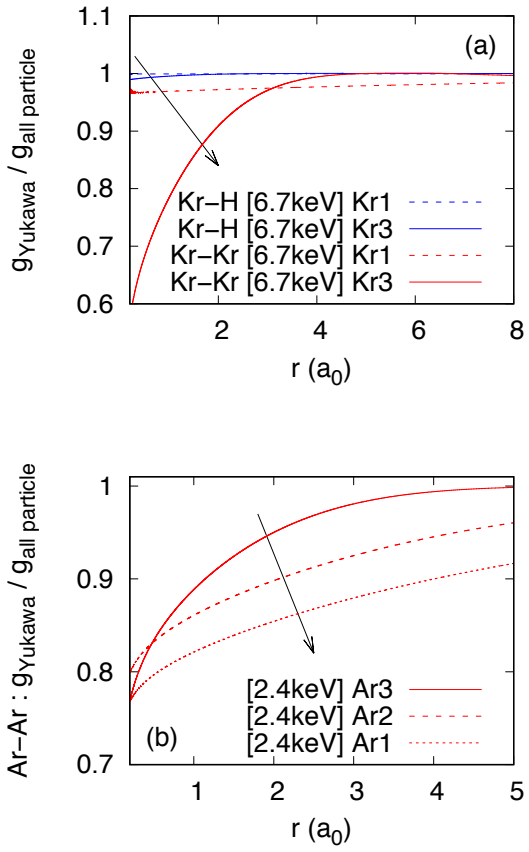
(a)
Kr–H [6.7keV] Kr1
Kr–H [6.7keV] Kr3
Kr–Kr [6.7keV] Kr1
Kr–Kr [6.7keV] Kr3
g_Yukawa / g_all particle
r (a_0)
(b)
[2.4keV] Ar3
[2.4keV] Ar2
[2.4keV] Ar1
Ar–Ar : g_Yukawa / g_all particle
r (a_0)

Figure 9

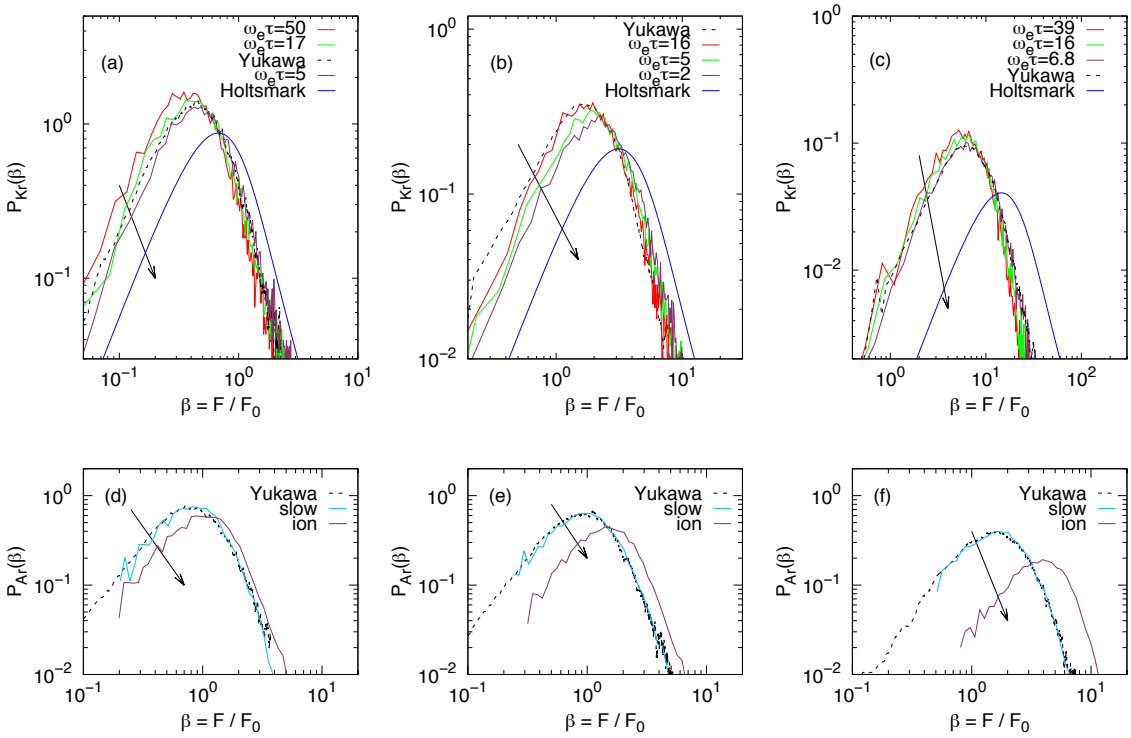
(a)
ωeτ=50
ωeτ=17
Yukawa
ωeτ=5
Holtsmark
PKr(β)
β = F / F0
(b)
Yukawa
ωeτ=16
ωeτ=5
ωeτ=2
Holtsmark
PKr(β)
β = F / F0
(c)
ωeτ=39
ωeτ=16
ωeτ=6.8
Yukawa
Holtsmark
PKr(β)
β = F / F0
(d)
Yukawa
slow
ion
PAr(β)
β = F / F0
(e)
Yukawa
slow
ion
PAr(β)
β = F / F0
(f)
Yukawa
slow
ion
PAr(β)
β = F / F0

Figure 10

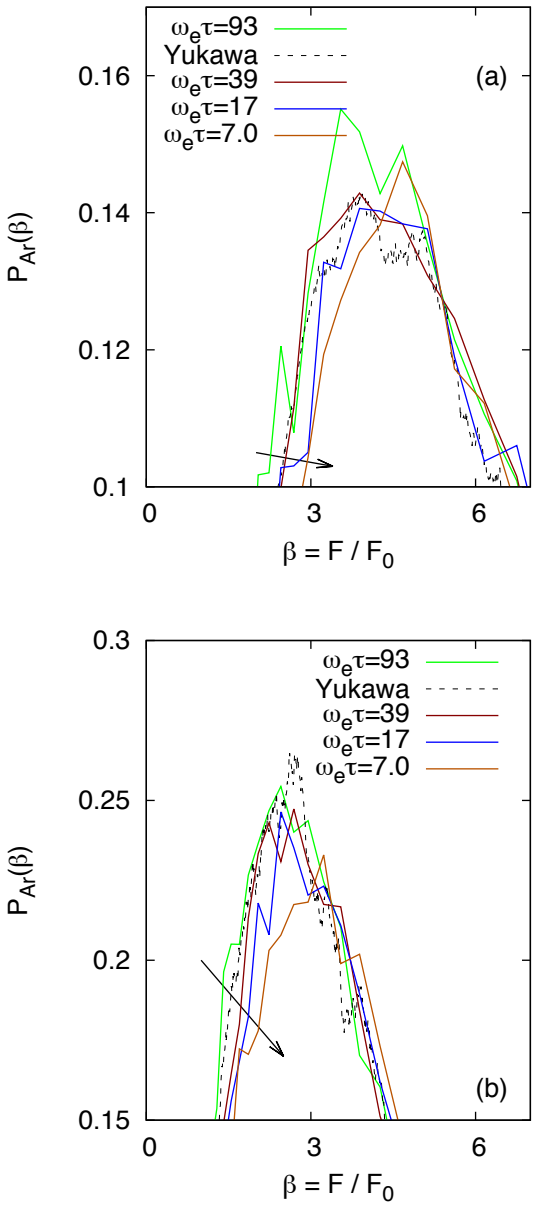
ωeτ=93
Yukawa
ωeτ=39
ωeτ=17
ωeτ=7.0
(a)
0.16
0.14
0.12
0.1
PAr(β)
0
3
6
β = F / F0
0.3
0.25
0.2
0.15
(b)

Figure 11

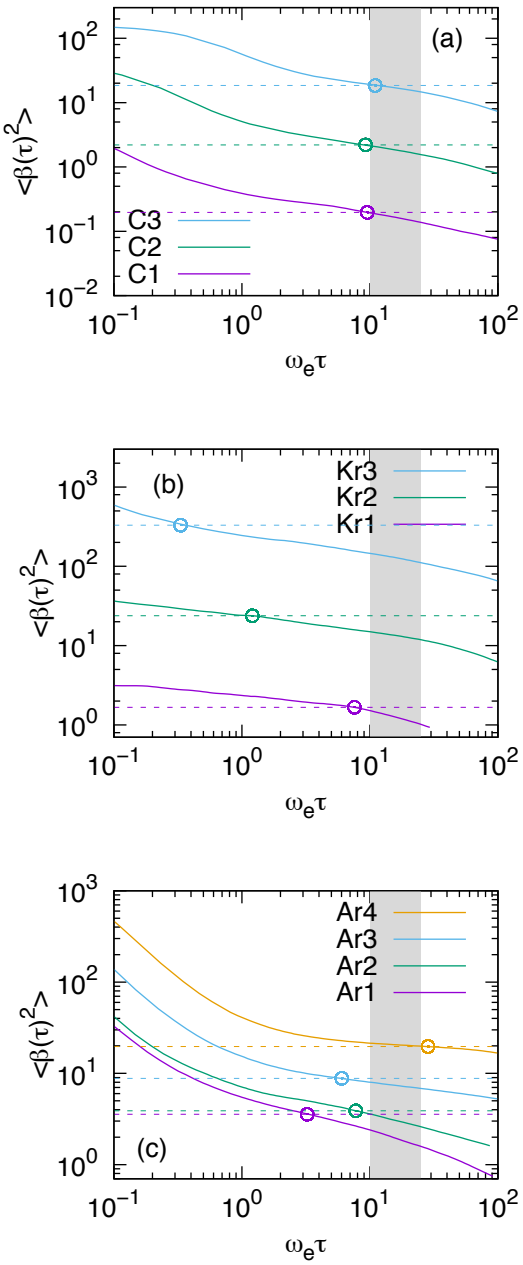
(a)
C3
C2
C1
$<\beta(\tau)^2>$
$\omega_e\tau$
(b)
Kr3
Kr2
Kr1
$<\beta(\tau)^2>$
$\omega_e\tau$
(c)
Ar4
Ar3
Ar2
Ar1
$<\beta(\tau)^2>$
$\omega_e\tau$

Figure 12

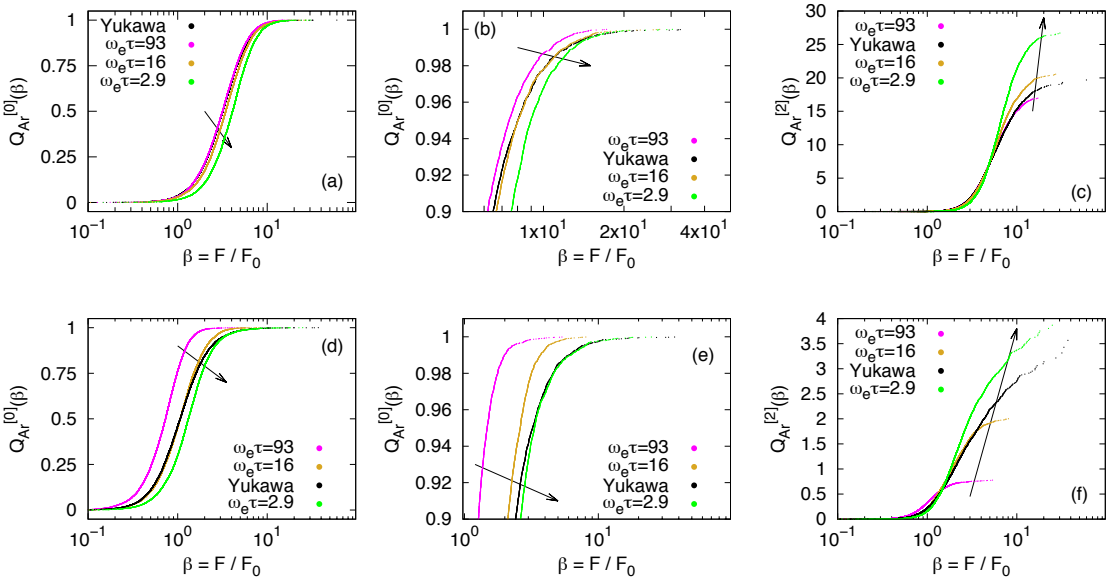

Figure 13